CrossMark

The DESI Bright Galaxy Survey: Final Target Selection, Design, and Validation

ChangHoon Hahn[1,2] , Michael J. Wilson[2,3] , Omar Ruiz-Macias[3] , Shaun Cole[3] , David H. Weinberg[4] , John Moustakas[5] , Anthony Kremin[2] , Jeremy L. Tinker[6] , Alex Smith[3,7,8] , Risa H. Wechsler[9,10,11] , Steven Ahlen[12] , Shadab Alam[8] , Stephen Bailey[2] , David Brooks[13] , Andrew P. Cooper[14] , Tamara M. Davis[15] , Kyle Dawson[16] , Arjun Dey[17] , Biprateep Dey[18] , Sarah Eftekharzadeh[19] , Daniel J. Eisenstein[20] , Kevin Fanning[21,22] , Jaime E. Forero-Romero[23] , Carlos S. Frenk[3] , Enrique Gaztañaga[24] , Satya Gontcho A Gontcho[2,25] , Julien Guy[2] , Klaus Honscheid[21] , Mustapha Ishak[26] , Stéphanie Juneau[27] , Robert Kehoe[28] , Theodore Kisner[2] , Ting-Wen Lan[29,30] , Martin Landriau[2] , Laurent Le Guillou[31] , Michael E. Levi[2] , Christophe Magneville[32] , Paul Martini[22,33] , Aaron Meisner[27] , Adam D. Myers[34] , Jundan Nie[35] , Peder Norberg[3,36] , Nathalie Palanque-Delabrouille[2,32] , Will J. Percival[37,38,39] , Claire Poppett[2], Francisco Prada[40] , Anand Raichoor[2] , Ashley J. Ross[22], Sasha Safonova[41], Christoph Saulder[42] , Eddie Schlafly[43] , David Schlegel[2] , David Sierra-Porta[23,44] , Gregory Tarle[45] , Benjamin A. Weaver[27], Christophe Yèche[32] , Pauline Zarrouk[31], Rongpu Zhou[2] , Zhimin Zhou[35] , and Hu Zou[35]

[1] Department of Astrophysical Sciences, Princeton University, Peyton Hall, Princeton, NJ 08544, USA; changhoon.hahn@princeton.edu
[2] Lawrence Berkeley National Laboratory, One Cyclotron Road, Berkeley, CA 94720, USA
[3] Institute for Computational Cosmology, Department of Physics, Durham University, South Road, Durham DH1 3LE, UK
[4] Department of Astronomy and the Center for Cosmology and Astroparticle Physics, The Ohio State University, 140 West 18th Avenue, Columbus, OH 43210, USA
[5] Department of Physics and Astronomy, Siena College, 515 Loudon Road, Loudonville, NY 12211, USA
[6] Center for Cosmology and Particle Physics, Department of Physics, New York University, New York, NY 10003, USA
[7] IRFU, CEA, Université Paris-Saclay, F-91191 Gif-sur-Yvette, France
[8] Institute for Astronomy, University of Edinburgh, Royal Observatory, Blackford Hill, Edinburgh EH9 3HJ, UK
[9] Department of Physics, Stanford University, 382 Via Pueblo Mall, Stanford, CA 94305, USA
[10] Kavli Institute for Particle Astrophysics and Cosmology, Stanford University, Stanford, CA 94305, USA
[11] SLAC National Accelerator Laboratory, Menlo Park, CA 94025, USA
[12] Physics Dept., Boston University, 590 Commonwealth Avenue, Boston, MA 02215, USA
[13] Department of Physics & Astronomy, University College London, Gower Street, London, WC1E 6BT, UK
[14] Institute of Astronomy and Department of Physics, National Tsing Hua University, 101 Kuang-Fu Rd. Sec. 2, Hsinchu 30013, Taiwan
[15] School of Mathematics and Physics, University of Queensland, 4101, Australia
[16] Department of Physics and Astronomy, The University of Utah, 115 South 1400 East, Salt Lake City, UT 84112, USA
[17] NSF's NOIRLab, 950 N. Cherry Avenue, Tucson, AZ 85719, USA
[18] Department of Physics & Astronomy and Pittsburgh Particle Physics, Astrophysics, and Cosmology Center (PITT PACC), University of Pittsburgh, 3941 O'Hara Street, Pittsburgh, PA 15260, USA
[19] Universities Space Research Association, NASA Ames Research Centre, USA
[20] Center for Astrophysics | Harvard & Smithsonian, 60 Garden Street, Cambridge, MA 02138, USA
[21] Department of Physics, The Ohio State University, 191 West Woodruff Avenue, Columbus, OH 43210, USA
[22] Center for Cosmology and AstroParticle Physics, The Ohio State University, 191 West Woodruff Avenue, Columbus, OH 43210, USA
[23] Departamento de Física, Universidad de los Andes, Cra. 1 No. 18A-10, Bogotá, Colombia
[24] Institut de Ciencies de l'Espai, IEEC-CSIC, Campus UAB, Carrer de Can Magrans s/n, E-08913 Bellaterra, Barcelona, Spain
[25] Department of Physics and Astronomy, University of Rochester, 500 Joseph C. Wilson Boulevard, Rochester, NY 14627, USA
[26] Department of Physics, The University of Texas at Dallas, Richardson, TX 75080, USA
[27] NSF's National Optical-Infrared Astronomy Research Laboratory, 950 N. Cherry Avenue, Tucson, AZ 85719, USA
[28] Department of Physics, Southern Methodist University, 3215 Daniel Avenue, Dallas, TX 75275, USA
[29] Department of Physics, National Taiwan University, Taipei 10617, Taiwan
[30] Graduate Institute of Astrophysics, National Taiwan University, Taipei 10617, Taiwan
[31] Sorbonne Université, Université Paris Diderot, CNRS/IN2P3, Laboratoire de Physique Nucléaire et de Hautes Energies, LPNHE, 4 place Jussieu, F-75252 Paris, France
[32] CEA Saclay, IRFU F-91191 Gif-sur-Yvette, France
[33] Department of Astronomy, The Ohio State University, 4055 McPherson Laboratory, 140 W. 18th Avenue, Columbus, OH 43210, USA
[34] Department of Physics & Astronomy, University of Wyoming, 1000 E. University, Dept. 3905, Laramie, WY 82071, USA
[35] National Astronomical Observatories, Chinese Academy of Sciences, A20 Datun Rd., Chaoyang District, Beijing, 100101, People's Republic of China
[36] Center for Extragalactic Astronomy, Department of Physics, Durham University, South Road, Durham DH1 3LE, UK
[37] Waterloo Centre for Astrophysics, University of Waterloo, 200 University Avenue W, Waterloo, ON N2L 3G1, Canada
[38] Department of Physics and Astronomy, University of Waterloo, 200 University Avenue W, Waterloo, ON N2L 3G1, Canada
[39] Perimeter Institute for Theoretical Physics, 31 Caroline Street N, Waterloo, ON N2L 2Y5, Canada
[40] Instituto de Astrofísica de Andalucía (CSIC), Glorieta de la Astronomía, s/n, E-18008 Granada, Spain
[41] Physics Department, Yale University, P.O. Box 208120, New Haven, CT 06511, USA
[42] Korea Astronomy and Space Science Institute, 776, Daedeokdae-ro, Yuseong-gu, Daejeon 34055, Republic of Korea
[43] Lawrence Livermore National Laboratory, P.O. Box 808 L-211, Livermore, CA 94551, USA
[44] Facultad de Ciencias Básicas. Universidad Tecnológica de Bolívar. Cartagena 130010, Colombia
[45] Department of Physics, University of Michigan, Ann Arbor, MI 48109, USA

Abstract

Over the next 5 yr, the Dark Energy Spectroscopic Instrument (DESI) will use 10 spectrographs with 5000 fibers on the 4 m Mayall Telescope at Kitt Peak National Observatory to conduct the first Stage IV dark energy galaxy survey. At $z < 0.6$, the DESI Bright Galaxy Survey (BGS) will produce the most detailed map of the universe during the dark-energy-dominated epoch with redshifts of >10 million galaxies spanning 14,000 deg^2. In this work, we present and validate the final BGS target selection and survey design. From the Legacy Surveys, BGS will target an $r < 19.5$ mag limited sample (BGS Bright), a fainter $19.5 < r < 20.175$ color-selected sample (BGS Faint), and a smaller low-z quasar sample. BGS will observe these targets using exposure times scaled to achieve homogeneous completeness and cover the footprint three times. We use observations from the Survey Validation programs conducted prior to the main survey along with simulations to show that BGS can complete its strategy and make optimal use of "bright" time. BGS targets have stellar contamination $<1\%$, and their densities do not depend strongly on imaging properties. BGS Bright will achieve $>80\%$ fiber assignment efficiency. Finally, BGS Bright and BGS Faint will achieve $>95\%$ redshift success over any observing condition. BGS meets the requirements for an extensive range of scientific applications. BGS will yield the most precise baryon acoustic oscillation and redshift-space distortion measurements at $z < 0.4$. It presents opportunities for new methods that require highly complete and dense samples (e.g., N-point statistics, multitracers). BGS further provides a powerful tool to study galaxy populations and the relations between galaxies and dark matter.

Unified Astronomy Thesaurus concepts: Observational cosmology (1146); Cosmology (343); Redshift surveys (1378); Galaxies (573); Galactic and extragalactic astronomy (563); Galaxy spectroscopy (2171); Spectro-photometry (1556)

1. Introduction

The Dark Energy Spectroscopic Instrument (DESI;[46] DESI Collaboration et al. 2016a) is a spectroscopic galaxy survey designed to accurately measure cosmic acceleration and determine the nature of dark energy. On seeing first light on 2019 October 22, DESI made a significant leap in becoming the first "Stage IV" (Albrecht et al. 2006) dark energy experiment to be realized.[47] Observations are taken with the 4 m Mayall telescope at Kitt Peak National Observatory with a focal plane filled with robotically actuated fibers that simultaneously direct the light of 5000 galaxies to a set of 10 optical spectrographs (360 nm $< \lambda <$ 980 nm with a spectral resolution of $2000 < \lambda/\Delta\lambda < 5500$).

Over the next 5 yr of operations, DESI will conduct the Bright Galaxy Survey (BGS) of more than 10 million galaxies over the redshift range $0 < z < 0.6$, alongside a dark-time redshift survey of 20 million luminous red galaxies (LRGs), emission-line galaxies (ELGs), and quasars (DESI Collaboration et al. 2016a). From the three-dimensional spatial clustering of these galaxies and quasars, DESI will precisely measure the expansion history of the universe using baryon acoustic oscillations (BAO) and the growth of structure using redshift-space distortions (RSDs). With an expected footprint of 14,000 deg^2 and longer redshift baseline, DESI will achieve a precision 1–2 orders of magnitude better than that of existing surveys (Levi et al. 2013).

While the dark-time survey delivers informative constraints at high redshift, BGS will probe the epoch when dark energy becomes dominant and its impact is expected to be greatest. BGS presents a unique opportunity to probe lower-redshift regimes, where model predictions vary most strongly among theories of modified gravity and dark energy. As an added benefit, BGS can proceed in some of the slowest observing conditions available, since galaxies are brighter at shorter distances, and optimize the use of bright time. The main BGS sample (BGS Bright) constitutes an $r < 19.5$ mag limited sample that is an order of magnitude larger than that of the Sloan Digital Sky Survey I and II combined (SDSS; York et al. 2000). A sample of fainter $19.5 < r < 20.175$ galaxies (BGS Faint), color selected to achieve high redshift efficiency, ensures that BGS will be the highest-density DESI tracer and deliver the highest-fidelity measurement of the density field. Meanwhile, the lower-redshift quasar sample (BGS active galactic nuclei (AGNs); S. Juneau et al. 2023, in preparation) ensures that the quasar sample obtained by DESI is as complete as possible. With these samples, BGS will provide a galaxy sample that will be more than 10 times the density of the LOWZ SDSS-III (Eisenstein et al. 2011) Baryon Oscillation Spectroscopic Survey (BOSS; Dawson et al. 2013) and up to 2 mag fainter than the SDSS Main Galaxy Survey (MGS; Strauss et al. 2002), with double the median redshift ($z \approx 0.2$).

For dark energy science, BGS will achieve the best measurement of BAO and RSD at redshifts $z \leqslant 0.4$ to date. The lower redshift of BGS will provide maximum leverage against high-redshift measurements and constraints from cosmic microwave background (CMB) observations. BGS will also enable new approaches to measuring the growth of structure, including the use of galaxy groups and clusters (Mohammad et al. 2016), galaxy–galaxy weak lensing (Heymans et al. 2021; Miyatake et al. 2022; Abbott et al. 2022; Amon et al. 2022), higher-order statistics (Gil-Marín et al. 2017), small-scale clustering (Zhai et al. 2019), and a range of complementary techniques. Its exceptionally high sampling density and wide selection also open the door to innovative techniques such as "multitracer" methods that exploit galaxy populations with different clustering properties (e.g., McDonald & Seljak 2009; Seljak 2009; Blake et al. 2013; Wang & Zhao 2020) and methods that forward model the small-scale density field (e.g., Seljak et al. 2017). More rigorous tests of systematic effects based on, for instance, splits by galaxy type (Ross et al. 2014) will also be possible with BGS. Beyond dark energy, BGS will also enable novel tests of modified gravity theories using the velocity fields of

---

[46] We will use DESI to interchangeably refer to the instrument and the cosmological surveys conducted with it.

[47] Stage IV represents experiments that will increase the figure of merit in the Albrecht et al. (2006) Dark Energy Task Force report by at least an order of magnitude over Stage II experiments (ongoing dark energy projects at the time of the report).

cluster infall regions (Zu et al. 2014) and precise measurements of the sum of neutrino masses with higher-order clustering (Hahn & Villaescusa-Navarro 2021) and other statistics.

The BGS will also provide an extraordinary resource for advancing our understanding of the physical processes that drive galaxy formation and evolution. With spectra and photometry for each of its >10 million galaxies, BGS will enable measurements of their physical properties (Hahn et al. 2023) and provide the most precise measurements of galaxy property statistics at low redshifts, e.g., the stellar mass function (Li & White 2009; Moustakas et al. 2013), the star-forming sequence (Noeske et al. 2007), and the mass–metallicity relation (Tremonti et al. 2004). It will also enable studies of galaxy groups (Eke et al. 2004), the connection between galaxies and dark matter (Tinker et al. 2011; Zu & Mandelbaum 2015; Xu et al. 2018), and the environment-dependent luminosity function (McNaught-Roberts et al. 2014; Eardley et al. 2015; Fang et al. 2019). By extending to faint apparent magnitudes $r < 20.175$, which corresponds to galaxies of stellar mass $\sim 10^7\ M_\odot$ at $z < 0.025$ (Hahn et al. 2023), BGS will also be an unprecedented sample for studying dwarf galaxies (Mao et al. 2021).

To achieve the broad range of science goals with BGS, we establish the following requirements for the survey. BGS will (a) sample a wide range of galaxy types, (b) have a high and well-characterized completeness, and (c) be at least an order of magnitude larger than the largest comparable survey that exists today (SDSS MGS; 10^6 galaxies). For (a), we require the BGS Bright sample to be selected using a magnitude limit and to have high target density, above >800 targets deg^{-2}. For (b) and (c), we require that BGS targets have <1% stellar contamination rates, that >80% of them are assigned to a fiber, and that >95% of those assigned produce successful redshifts. This ensures that we successfully assign fibers to and measure redshifts for the vast majority of galaxies targeted. Lastly, we require a 20% margin in the forecasted BGS operations to ensure that DESI will be able to complete the survey even with unforeseen events.

In this paper, we present the final target selection, design, and validation of the BGS. We demonstrate that the choices we make for BGS will achieve all of the stated requirements and can be executed in the bright time available over the 5 yr of DESI operations. This work presents significant updates and new results from preliminary versions of the BGS target selection presented by Ruiz-Macias et al. (2021) and Zarrouk et al. (2021). These advancements are based on early spectroscopic observations from the Survey Validation (SV) programs conducted by DESI prior to the main survey. SV was conducted between 2020 December and 2021 May with the primary goal of verifying that each survey meets and exceeds its requirements. Complementary papers describe the target selection for the dark-time DESI tracers (LRGs; Zhou et al. 2023; ELGs; A. Raichoor et al. 2023, in preparation; and QSOs; Chaussidon et al. 2023) and the Milky Way Survey (MWS; Cooper et al. 2023). Myers et al. (2023) present how the target selections are implemented in DESI. DESI Collaboration et al. (2023, in preparation) presents an overview of the DESI spectroscopic observations. Lan et al. (2023) and Alexander et al. (2023) present the visual inspection for the galaxies (BGS, LRG, ELG) and QSO targets, respectively, used to construct spectroscopic truth tables.

In Section 2, we describe the latest imaging data from the Legacy Surveys (Dey et al. 2019) and external catalogs that are used for the BGS target selection. We describe the specific selection criteria for each of the BGS samples in Section 3. In Section 4, we describe and explain the details of the BGS survey design and observing strategy. We describe the SV programs in detail in Section 5.1 and present the validation of the target selection (Section 5.2), redshift success (Section 5.3), and fiber assignment efficiency (Section 5.4). Finally, we showcase the BGS samples for the first public data set in Section 6 and summarize our conclusions in Section 7. We assume AB magnitudes and a flat Λ cold dark matter (ΛCDM) cosmology described by the final Planck results (Planck Collaboration et al. 2020): $\omega_b = 0.02237$, $\omega_{\rm cdm} = 0.12$, $h = 0.6736$, $A_s = 2.083 \times 10^{-9}$, $n_s = 0.9649$.

2. Imaging Data

The target selection for BGS is primarily based on the imaging data from the Legacy Surveys (LS). We also make use of observations from a number of external catalogs derived from Gaia Data Release 2 (Gaia Collaboration et al. 2016), Tycho-2 (Høg et al. 2000), and the Siena Galaxy Atlas (SGA; Moustakas et al. 2021; J. Moustakas et al. 2023, in preparation). In the following we briefly describe each of these imaging surveys.

2.1. Legacy Survey Data Release 9

The DESI Legacy Imaging Surveys[48] (also known as the Legacy Surveys; LS) comprise the primary photometric catalog that we use for our target selection (Dey et al. 2019). LS covers $\sim$14,000 deg^2 of the extragalactic sky visible from the northern hemisphere split into two contiguous areas by the Galactic plane, together with $\sim$6000 deg^2 of the southern sky. It provides photometry with the necessary coverage, depth, and target density for DESI. For BGS we use the ninth data release: LS DR9 (D. Schlegel et al. 2023, in preparation). In Figure 1, we present the footprint of the LS imaging in gray.

LS provides photometry in three optical bands, g (470 nm), r (623 nm), and z (913 nm), and is observed using three independent programs: the Beijing–Arizona Sky Survey (BASS; Zou et al. 2017), the Mayall z-band Legacy Survey (MzLS), and the Dark Energy Camera Legacy Survey (DECaLS). BASS observed g- and r-band photometry using the 2.3 m Bok telescope over $\sim$5100 deg^2 of the northern Galactic cap (NGC) above decl. > 32°.375. MzLS observed z-band photometry over the same footprint as BASS using the 4 m Mayall telescope. Lastly, DECaLS observed g-, r-, and z-band photometry over the rest of the LS footprint using the Dark Energy Camera (DECam; Flaugher et al. 2015) on the 4 m Blanco telescope. DECaLS expands on the footprint of the Dark Energy Survey (DES; Dark Energy Survey Collaboration et al. 2016), for which DECam was initially built, using publicly available DECam time. The optical photometries from these surveys are complemented by infrared Wide-field Infrared Survey Explorer (WISE; Wright et al. 2010) $W1$ (3.4 μm) and $W2$ (4.6 μm) photometry from the custom "unWISE" catalog (Meisner et al. 2017b). The infrared photometry is derived from all WISE imaging through year 6 of the NEOWISE Reactivation, force-photometered at the locations of the LS optical sources (Meisner et al. 2017a).

---

[48] https://www.legacysurvey.org/dr9/
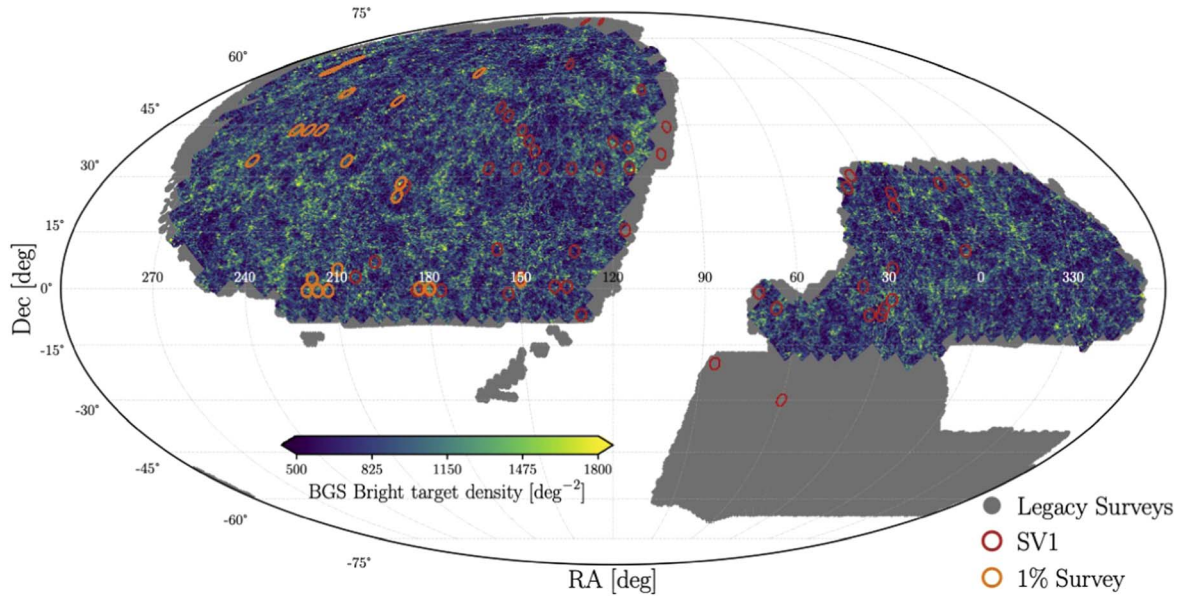
Figure 1. The 14,000 deg^2 footprint for the DESI BGC (color map). Imaging from the Legacy Surveys DR9 allows the selection of BGS targets over a larger area, approximately 20,000 deg^2 (gray). The color map represents the density of BGS Bright targets (Section 3.1). During the SV phases of operations, DESI observed SV1 and the One-Percent Survey to optimize and validate the BGS target selection and survey performance. We mark the tiles observed during SV1 and the One-Percent Survey in red and orange, respectively.

All data from LS are first reduced using the National Optical-Infrared Astronomy Research Laboratory (NOIR-Lab) DECam Community Pipeline,[49] which provides instrumental calibration, astrometric calibration, photometric characterization, and masking of various artifacts. Afterward, the LS source catalog is constructed using the LEGACYPIPE[50] pipeline, which uses the TRACTOR[51] software (Lang et al. 2016) for pixel-level forward modeling of astronomical sources. LEGACYPIPE initially detects sources and defines contiguous sets of pixels associated with each detection. TRACTOR then fits these pixels with surface brightness models (e.g., point source, de Vaucouleurs galaxy profile) on individual optical images (g, r, and z bands), taking into account their different point-spread function (PSF) and sensitivity. Based on a penalized χ^2, LEGACYPIPE then determines which surface brightness model best describes the light profile and whether to keep the source in the catalog.

The resulting LS source catalog includes source positions, fluxes, r-band fiber flux, and measures of the quality of the source fits. The fluxes correspond to total model flux, while fiber flux represents the predicted flux within a $1\farcs5$-diameter fiber aperture in Gaussian seeing with an FWHM of $1''$. It also provides galactic extinction measurements derived from the Schlegel et al. (1998; SFD98) maps. For a fiducial galaxy target, defined as a source with an exponential profile with half-light radius of $0\farcs45$, LS achieves a median 5σ detection limit in the g, r, and z bands of 23.72, 23.27, and 22.22 mag over the DECaLS coverage and 23.48, 22.87, and 22.29 mag for BASS/MzLS. The value of $0\farcs45$ corresponds to the median source size of DESI targets. For more details on the LS imaging data, we refer readers to Zou et al. (2017), Dey et al. (2019), and D. Schlegel et al. (2023, in preparation).

In addition to the small differences in the detection limits between DECaLS and BASS, there are also slight differences in their measured magnitudes due to the fact that they were observed using different instruments at different telescopes. Zarrouk et al. (2021) quantified this discrepancy in detail using some of the overlapping region between DECaLS and BASS in the NGC over the range $29° < \mathrm{decl.} < 35°$. Overall, the same objects are slightly brighter in the r band in DECaLS versus BASS. To account for this discrepancy, we impose an r-band magnitude offset of $\Delta r = r_{\mathrm{BASS}} - r_{\mathrm{DECaLS}} = 0.04$ mag in our target selection. We opt for a simple magnitude offset, instead of a color-dependent one, because it sufficiently accounts for the discrepancy, without imposing a single color correction on galaxies over the entire broad r range. The amplitude of the offset is determined so that the average target density of BGS Bright targets (Section 3.2) in BASS is equal to the average target density in DECaLS. For more details on the magnitude offsets between DECaLS and BASS, we refer readers to Zarrouk et al. (2021).

2.2. External Catalogs

In addition to the LS imaging, we use additional catalogs in the BGS sample selection for star–galaxy separation and spatial masking. We describe these catalogs below.

2.2.1. Gaia Data Release 2

Gaia is a European Space Agency space-based mission launched in 2013 with the goal of observing $\approx 1\%$ of all the stars in the Milky Way (Gaia Collaboration et al. 2016). In addition to accurate positions and proper motions of these stars, Gaia provides photometry in the G band, which covers the wavelength range 330–1050 nm (hereafter G_{Gaia}; Carrasco et al. 2016). The Gaia Data Release 2 (DR2; Gaia Collaboration et al. 2018), which covers 22 months of observations and was released on 2018 April, provides observations for 1.7 billion stars over the entire sky down to $G_{\mathrm{Gaia}} = 20.7$. Since Gaia is

sufficiently deep to detect stars that contaminate the BGS sample, we use it in our star–galaxy separation criteria (Section 3.1).

2.2.2. Tycho-2

Bright stars can often impact the measured photometric properties of nearby sources or cause spurious sources to be detected in imaging catalogs. We therefore exclude regions around bright stars in our sample selection to mitigate these effects (Section 3.1). For our list of bright stars, in addition to Gaia, we use the Tycho-2 catalog (Høg et al. 2000), which provides the few additional extremely bright stars missing from (or that have incorrect photometry in) Gaia. The Tycho-2 catalog contains the positions, proper motions, and photometry for 2.5 million of the brightest stars in the Milky Way.

2.2.3. Globular Clusters and Planetary Nebulae

The bright and extended profiles of globular clusters (GCs) and planetary nebulae (PNs) can impact our selection of extragalactic sources near them. We therefore mask the regions surrounding them in our sample selection (see Section 3.1 for details). For our catalog of GCs and PNs, we select all objects classified as GCs or PNs in the OpenNGC catalog[52] (Verga 2017). We also include nine additional GCs and compact open clusters from the literature, as well as two Local Group galaxies, Fornax and Sculptor. For further details on our list of GCs and PNs, we refer readers to the LS DR9 documentation[53] and D. Schlegel et al. (2023, in preparation).

2.2.4. Siena Galaxy Atlas

Images of large galaxies can often generate spurious sources in standard photometric pipelines. For instance, H II regions within a galaxy can be mistaken for individual sources. The outskirts of large galaxies can also be fragmented into spurious sources. To mitigate this contamination, we use the Siena Galaxy Atlas (SGA; Moustakas et al. 2021)[54] to select the largest galaxies in the LS. Using optical data from the HyperLeda catalog (Makarov et al. 2014) and infrared data from the ALLWISE catalog (Secrest et al. 2015), the SGA identified large galaxies with $D(25) > 20''$, where $D(25)$ is the diameter at the 25 mag arcsec^{-2} surface brightness isophote, a conventional measure of galaxy size. A separate source extraction was performed in regions around those galaxies in DR9. In total, the SGA catalog includes 383,620 galaxies with DR9 grz photometry.

3. Target Selection

Our ultimate goal is to construct BGS to have a highly complete, high-density sample of galaxies with robust redshift measurements that meets the DESI science requirements. This requires a reliable input target catalog derived from the LS and external catalogs. In this section, we describe how we construct this input target catalog for BGS (Section 3.1) and how we select targets from it for the BGS Bright, BGS Faint, and AGN samples (Sections 3.2, 3.3, and S. Juneau et al. 2023, in preparation). For additional details on the target selection, we refer readers to the DESI target selection pipeline paper

(Myers et al. 2023). The target catalog will be publicly available at the DESI Data Documentation website.[55]

3.1. Selection Cuts

We design the target catalog to ensure high efficiency and completeness for the redshift survey and remove any systematic effects that can affect galaxy clustering analyses. To achieve this, we minimize the number of spurious objects and impose spatial masking, star–galaxy separation, a fiber magnitude cut (FMC), a bright limit, and quality cuts on objects compiled from the LS and external catalogs. We describe each of these selection cuts below.

Spatial masking: We want to mask out regions of the sky surrounding bright stars, GCs, and PNs because these regions are typically contaminated by features such as extended halos, bleed trails, and diffraction spikes. These features in the imaging can not only compromise the photometry of surrounding objects but also produce spurious objects. For the BGS target catalog, we apply spatial masking around bright stars and GCs. First, for bright stars, we apply circular masks with a magnitude-dependent radius, R_{BS}. The masks account for the fact that TRACTOR underestimates galaxy fluxes near bright stars and thus reduce the target density in these regions. The masks are compiled using 773,673 Gaia DR2 (Section 2.2.1) objects with $G_{Gaia} < 13$ and 3349 Tycho-2 (Section 2.2.2) objects with visual magnitude brighter than MAG_VT < 13. The masks have radii

$$R_{BS}(m) = 815 \times 1.396^{-m} \text{ arcsec}, \tag{1}$$

where m is either G_{Gaia} or Tycho-2 MAG_VT magnitude. We use G_{Gaia} when both are available. We do not apply spatial masking around stars fainter than 13th magnitude. Next, for GCs, we apply a circular mask with radius defined by the major axis of the object. We apply this masking around all of the GCs and PNs in the list compiled from the OpenNGC catalog (Section 2.2.3). In total, our bright star and GC masks exclude 0.87% and 0.01% of the initial area, respectively.

We note that we do not apply spatial masking around large galaxies of the SGA (Section 2.2.4), unlike in the preliminary version of the target selection (Ruiz-Macias et al. 2021). Custom source fitting around the SGA galaxies in DR9 led to a significant improvement. Fits no longer automatically assume that the sources within $D(25)$ are best fit by a PSF model and thus more accurately measure their photometry. Since ~40%–50% of sources within the large galaxy mask are galaxies based on visual inspection and GAMA spectroscopy of overlapping galaxies (Zarrouk et al. 2021), we opt to reject spurious objects at a later stage.

Star–galaxy separation: For the BGS target catalog, we only want to include galaxies and exclude stars. To classify LS objects as either stars or galaxies, we use a combination of the photometric data from LS and Gaia DR2 (Section 2.2.1). An object is considered a BGS target if either of the following conditions are met:

1. object is not in the Gaia catalog;
2. object is in Gaia and has $(G_{Gaia} - r_{raw}) > 0.6$.

---

[52] https://github.com/mattiaverga/OpenNGC
[53] https://www.legacysurvey.org/dr9/external/
[54] https://sga.legacysurvey.org/

[55] Catalogs: https://data.desi.lbl.gov/public/ets/target/catalogs/; Documentation on the catalog directory structure: https://desidatamodel.readthedocs.io/en/latest/DESI_TARGET/TARG_DIR /index.html is available as part of the DESI data model: https://desidatamodel.readthedocs.io/en/latest/.
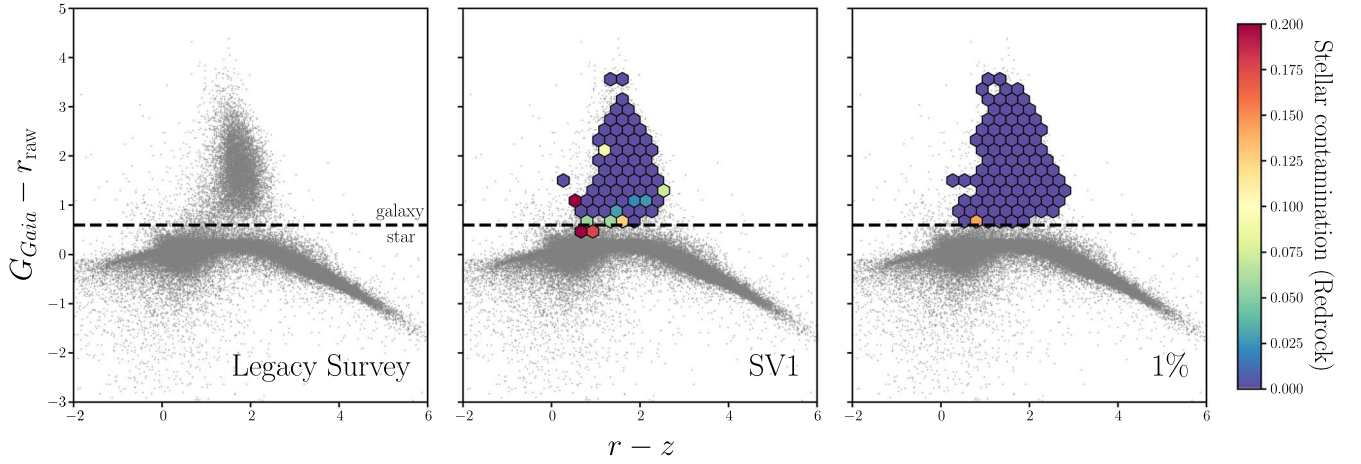
Figure 2. Star–galaxy separation in BGS is performed using a $G_{Gaia} - r_{raw}$ cut. This criterion exploits the fact that the Gaia magnitude is measured from space with a diffraction-limited PSF while the LS r magnitude captures the light from the entire source. LS objects (gray) with $G_{Gaia} - r_{raw} > 0.6$ (black dashed) or objects not in Gaia are classified as galaxies. G_{Gaia} is the G-band magnitude from Gaia DR2; r_{raw} is the LS r-band magnitude without Galactic extinction correction. In the middle and right panels, we present in the color maps the stellar contamination fraction for SV1 and the One-Percent Survey, respectively. The contamination fraction is estimated based on REDROCK spectral type classification and a minimum redshift cut, $z > 300$ km s^{-1}. We only include hexbins with at least 10 BGS targets. Stellar contamination is negligible ($<1\%$) above our star–galaxy separation threshold.

G_{Gaia} is the G-band magnitude from Gaia, and r_{raw} is the LS r-band magnitude that is *not* corrected for galactic extinction. Our ($G_{Gaia} - r_{raw}$) criterion takes advantages of the fact that G_{Gaia} is measured assuming that the object is a point source for a (narrow) diffraction-limited PSF measured from space. Hence, G_{Gaia} will be systematically fainter than the TRACTOR magnitudes for galaxies, which capture light from the entire galaxy. We use r_{raw} magnitudes because G_{Gaia} is also uncorrected for galactic extinction. Our star–galaxy separation has a significantly lower stellar contamination rate than the TRACTOR model classifications (Ruiz-Macias et al. 2021).

In the left panel of Figure 2, we present the ($r - z$) versus ($G_{Gaia} - r_{raw}$) distribution for LS objects (gray) and highlight our star–galaxy separation criterion (black dashed). Figure 2 clearly reveals the locus of galaxies in the color distribution above our ($G_{Gaia} - r_{raw}$) > 0.6 star–galaxy separation criterion.

Fiber magnitude cut: Some of the objects in the LS are imaging artifacts or fragments of "shredded" galaxies. In order to remove these spurious objects from our BGS target catalog, we apply the FMC below:

$$r_{fiber} < \begin{cases} 22.9 + (r - 17.8) & \text{for } r < 17.8 \\ 22.9 & \text{for } 17.8 < r < 20. \end{cases} \quad (2)$$

Here r_{fiber} is the r-band fiber magnitude derived from the predicted r-band flux of the object within a 1″.5-diameter fiber and r is the total r-band magnitude. In the left panel of Figure 3, we present our FMC (black dashed) in the r versus r_{fiber} distribution of LS objects. The bright end of the FMC is set so that it does not remove any spectroscopically confirmed GAMA galaxies. Meanwhile, the faint end of the FMC is determined through visual inspection of LS objects. The $r_{fiber} < 22.9$ limit rejects spurious objects and retains genuine galaxies. A total of 9.2 and 19.3 objects deg^{-2} are removed by the FMC in DECALS and BASS/MzLS, respectively.

Quality cuts: We want BGS Bright to be complete in all three optical bands of its imaging: g, r, and z. We therefore require that there is at least one photometric observation in each of the bands:

$$\text{nobs}_i > 0 \quad \text{for } i = g, r, z. \quad (3)$$

Here nobs$_i$ represents the number of observations (images) at the central pixel of the source in each band. This requirement removes 0.41% of the imaging footprint.

We also exclude spurious objects (e.g., imaging artifacts or stars) with extreme colors by requiring

$$-1 < (g - r) < 4 \quad (4)$$
$$-1 < (r - z) < 4. \quad (5)$$

The color cuts remove 3.44 and 25.7 objects deg^{-2} for DECALS and BASS/MzLS, respectively. A large fraction of these objects are the same as those removed by the FMC. We do not use any cuts based on TRACTOR photometric quality flags (unlike the preliminary Ruiz-Macias et al. 2021 selection), as they are not necessary for DR9.

Bright limit: Lastly, flux from very bright objects on neighboring fibers can contaminate the traces of faint objects on the spectrograph CCD and pollute their observed fluxes. This is particularly problematic at >9000 Å, where 10% of the flux of the contaminating source is scattered into the wings of its PSF. Since the faintest fiber magnitudes in BGS have $r_{fiber} \simeq 21.5$, we remove all objects that meet

$$(r > 12) \ \& \ (r_{fibertot} < 15) \quad (6)$$

from the BGS target catalog. Here $r_{fibertot}$ is the total fiber magnitude derived from the predicted r-band flux within a 1″.5-diameter fiber from all sources.[56] Most of the bright objects rejected by this threshold are stars and saturated point-like sources according to visual inspection. Based on similar concerns, MWS also applies a cut to the Milky Way sources sharing the focal plane (Cooper et al. 2023).

3.2. BGS Bright Sample

The highest-priority target class in BGS is a magnitude-limited "Bright" sample. From the sources that satisfy the selection cuts above, we impose an $r < 19.5$ mag limit to select the BGS Bright targets. With this simple selection, BGS Bright

---

[56] This ensures that if a bright object is modeled by multiple sources (shredding), then the intrinsic source will still be masked.
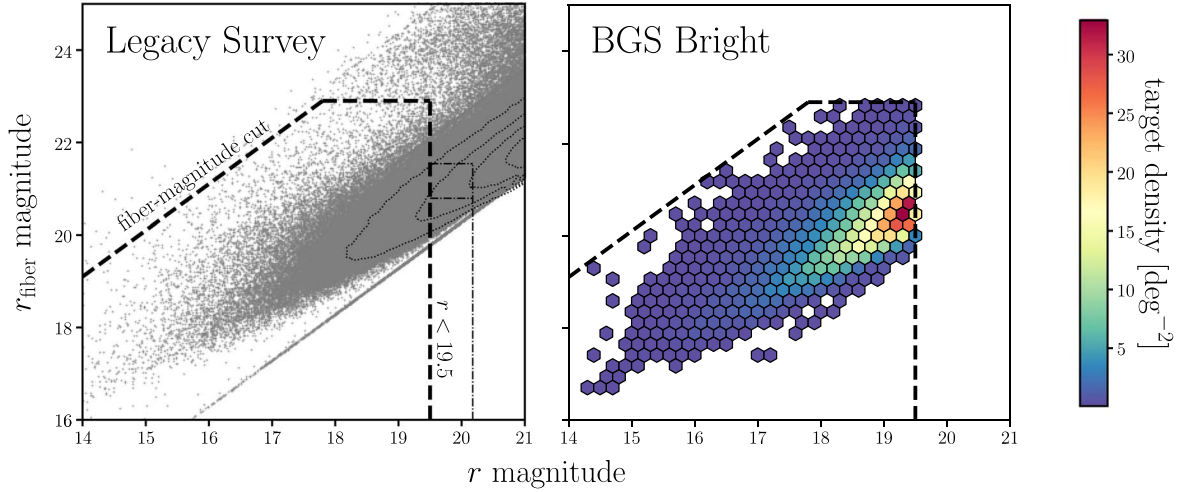
Figure 3. Targets for the BGS Bright sample are chosen based on the selection cuts described in Section 3.1 and an $r < 19.5$ magnitude cut. In the left panel, we show these cuts (based on fiber magnitude) and the $r < 19.5$ cut (black dashed) on the distribution of r vs. $r_{\rm fiber}$ magnitude for LS objects that pass our star–galaxy selection (gray). The contours mark the 11.7, 39.3, 67.5, and 86.4 percentiles of the distribution (dotted). We also include the r and $r_{\rm fiber}$ cuts for the BGS Faint sample (dotted–dashed). We impose selection cuts on BGS targets in order to minimize the number of spurious objects and mitigate any systematic effects that can affect galaxy clustering analyses. In the right panel, we present the target density of the BGS Bright targets (color map). In total, we have 864 targets deg^{-2} for the BGS Bright sample.

can achieve a range of scientific goals that require a dense sampling of galaxies and a wide range of galaxy properties. In the right panel of Figure 3, we present the target density of the BGS Bright sample as a function of r and $r_{\rm fiber}$ magnitudes. We represent the target density in each (r, $r_{\rm fiber}$) hexbin with the color map and mark the $r < 19.5$ mag limit (black dashed). We note that the locus of targets at low $r_{\rm fiber}$ with tightly correlated r and $r_{\rm fiber}$ are a small fraction of targets that are likely stellar contaminants. In total, we have 864 targets deg^{-2} for the BGS Bright sample. These targets can be accessed in DESI catalogs as described in Myers et al. (2023) under the `BGS_BRIGHT` bit name.

3.3. BGS Faint Sample

In addition to BGS Bright, BGS includes galaxies with magnitudes fainter than $r > 19.5$. This fainter sample will substantially increase the overall BGS target density and thus enable small-scale clustering measurements with higher signal-to-noise ratio (S/N). The BGS Faint sample will also enable multitracer analyses using multiple populations of tracers with very different biases, which are forecasted to produce the tightest constraints on RSD (McDonald & Seljak 2009; Seljak 2009; Wang & Zhao 2020). It will also include many faint emission-line galaxies that will be valuable for studies of galaxy evolution and the cosmic star formation history.

The preliminary BGS target selection described by Ruiz-Macias et al. (2021) only included an r-band magnitude cut. This selection, however, included many faint galaxies with low fiber fluxes, which significantly reduce the redshift success rate of the sample. In order to maintain high redshift efficiency and completeness, the final BGS Faint selection includes the following $r_{\rm fiber}$−color cut:

$$r_{\rm fiber} < \begin{cases} 20.75 & \text{if } (z - W1) - 1.2(g - r) + 1.2 < 0 \\ 21.5 & \text{if } (z - W1) - 1.2(g - r) + 1.2 \geqslant 0. \end{cases} \quad (7)$$

Here $W1$ is the magnitude in the WISE $W1$ band, 3.4 μm at 6″.1 angular resolution. We also include a 19.5 mag $< r <$ 20.175 mag limit in order to satisfy a $\sim$ 1400 target deg^{-2} constraint on

the total target density imposed by the survey fiber budget allocated to BGS. The corresponding fiber budget for the MWS stellar targets is $\sim$800 targets deg^{-2} (Cooper et al. 2023).

In a sample of LS-matched emission-line galaxies from the AGN and Galaxy Evolution Survey (AGES; Moustakas et al. 2011; Kochanek et al. 2012), we identified that Hα- and Hβ-emitting star-forming galaxies predominantly lie above a $(z - W1) - 1.2(g - r) + 1.2$ locus. This selection identifies galaxies that either have brighter fiber magnitudes or have emission lines in their spectra. As we discuss in Section 5, the high redshift success rate of this sample validates this selection. In the left panel of Figure 4, we present the $r_{\rm fiber}$ versus $(z - W1) - 1.2(g - r) + 1.2$ color distribution of LS objects that pass our star–galaxy selection (gray) and highlight the BGS Faint $r_{\rm fiber}$−color cut (black dashed). In the right panel of Figure 4, we present the number density of BGS Faint sample targets. We also mark the Equation (7) $r_{\rm fiber}$ and the 19.5 mag $< r <$ 20.175 mag limits in the r versus $r_{\rm fiber}$ distribution of LS objects in Figure 3 (dotted–dashed). In total, we have 533 targets deg^{-2} for the BGS Faint sample. These targets can be accessed in DESI catalogs as described in Myers et al. (2023) under the `BGS_FAINT` bit name.

3.4. BGS AGN Sample

In addition to the Bright and Faint samples, BGS includes a supplementary selection to recover AGN host galaxies that are rejected by the $(G_{\rm Gaia} - r_{\rm raw}) > 0.6$ star–galaxy separation cut but would otherwise pass BGS selection criteria. This BGS AGN sample is designed to increase the completeness of the DESI dark-time quasar targets. It does not overlap with the BGS Bright or Faint samples, by design, and has minimal overlap with the dark-time quasar targets because we remove $r > 17.5$ targets with a PSF morphological type.

To select targets with AGNs, we exploit optical and infrared colors that trace the signatures of hot, AGN-heated dust in the spectral energy distribution. The primary AGN selection
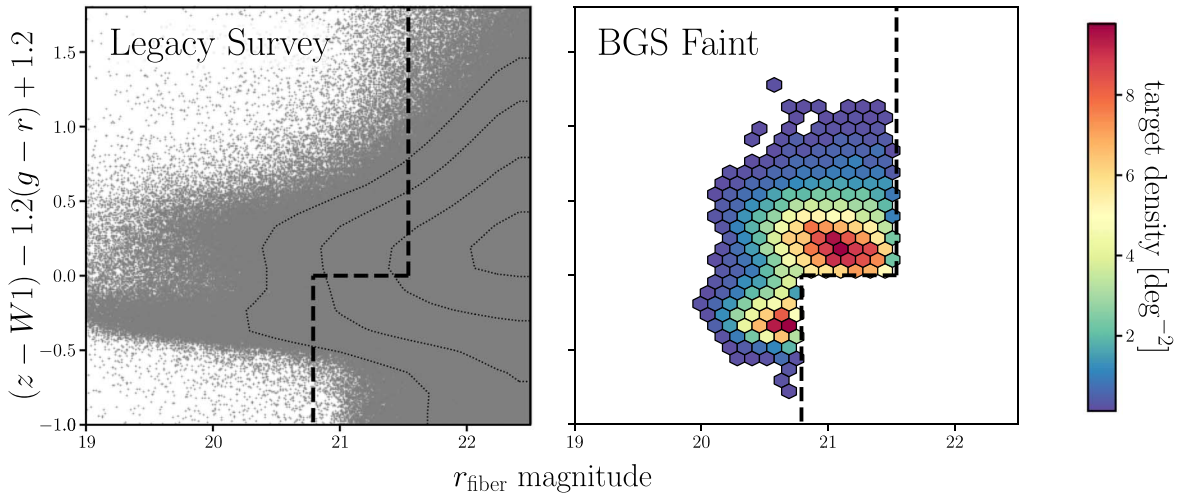
Figure 4. BGS Faint targets include objects fainter than BGS Bright, 19.5 mag $< r <$ 20.175 mag, that are within custom $r_{\rm fiber}-$color selection cuts (Equation (7)). In the left panel, we show the $r_{\rm fiber}-$color cut (black dashed) on the $r_{\rm fiber}$ vs. $(z - W1) - 1.2(g - r) + 1.2$ distribution of LS objects that pass our star–galaxy separation (gray). The contours mark the 11.7, 39.3, 67.5, and 86.4 percentiles of the distribution (dotted). Here $(z - W1) - 1.2(g - r) + 1.2$ is a proxy for the strength of Hα and Hβ, so BGS Faint targets either have bright fiber magnitudes or strong emission lines. We impose the $r_{\rm fiber}-$color cut in order to maintain high redshift efficiency for BGS Faint. In the right panel, we present the target density of the BGS Faint targets (color map). In total, we have 533 targets deg^{-2} for the BGS Faint sample.

criteria are

$$(z - W2) - (g - r) > -0.5 \tag{8}$$

$$(z - W1) - (g - r) > -0.7 \tag{9}$$

$$(W1 - W2) > -0.2 \tag{10}$$

$$(G_{\rm Gaia} - r) < 0.6. \tag{11}$$

We also require an $S/N > 10$ detection in both $W1$ and $W2$ bands to ensure a robust constraint in the infrared regime, and we apply quality and magnitude cuts. The full sample selection is described in a dedicated BGS AGN paper (S. Juneau et al. 2023, in preparation). The resulting target density of BGS AGNs is $\sim$3–4 targets deg^{-2}, distributed uniformly over the DESI footprint. These targets can be accessed in DESI catalogs as described in Myers et al. (2023) under the `BGS_WISE` bit name.

4. Survey Design

In this section, we present the final design of the BGS. We describe how we determine exposure times to achieve uniform >95% redshift efficiency for BGS exposures spanning a broad range of observing conditions (Section 4.1). We then present the observing strategy that BGS will employ to observe a footprint of 14,000 deg^2 with >80% fiber assignment completeness and 20% operational margins (Section 4.2). Lastly, we present the strategy for assigning fibers to BGS targets (Section 4.3).

4.1. Nominal Exposure Time

We want BGS to achieve near-homogeneous completeness in the final survey. This requires BGS exposures, which are taken over a broad range of observing conditions, to have uniform redshift efficiencies. To achieve this uniformity, exposure times are dynamically scaled by the Exposure Time Calculator (ETC), depending on the measured sky background, seeing, and transparency. For instance, an exposure taken close to the Moon with bright sky background will require a longer exposure time than an exposure taken at larger Moon

separation. We define the anchoring *nominal* exposure time as the exposure time required to achieve >95% redshift efficiency for the BGS Bright sample during nominal dark conditions, which roughly corresponds to the median expected conditions during dark time.[57]

We use spectral simulations to determine an initial estimate of the nominal exposure time. We construct multiple sets of simulated spectra using a range of exposure times and then select the exposure time that achieves >95% redshift efficiency. To construct these spectra, we first compile a catalog of GAMA galaxies that would be selected as BGS targets. We match each galaxy to a continuum template, constructed from galaxy spectra of AGES based on their redshift, r-band absolute magnitude, and $(g - r)$ color. Next, we add emission lines to the continuum using emission-line flux and width measurements from GAMA. We then normalize the simulated spectra to match the fiber aperture flux from LS, because DESI spectra only include light within the fiber aperture. We construct 1000 simulated spectra in total that cover the full range of BGS galaxy spectral types.

From the noiseless galaxy spectra, we construct realistic DESI-like spectra using the DESI `specsim` package[58] (Kirkby et al. 2021), which simulates the source profile, atmosphere, and DESI instrument characteristics. The atmosphere model accounts for the variance added to the source spectrum (i.e., our noiseless galaxy spectra) from the sky emission spectrum and the attenuation of the spectrum by its passage through the atmosphere. In our case, we use the dark sky spectrum derived from UVES (Hanuschik 2003) and the nominal air mass for the attenuation. The total photon count entering the fiber is then modeled using the spectrum and specified exposure time. Afterward, the DESI instrument model simulates the resolution effects and throughput for each of the three spectrograph cameras. Finally, the sensor electronics

---

[57] The nominal dark condition is defined at zenith ($X = 1$), with no extinction ($E(B - V) = 0.0$), a seeing FWHM of $1''1$, and a sky background of $r = 21.07$ mag arcsec^{-2}.
[58] https://specsim.readthedocs.io
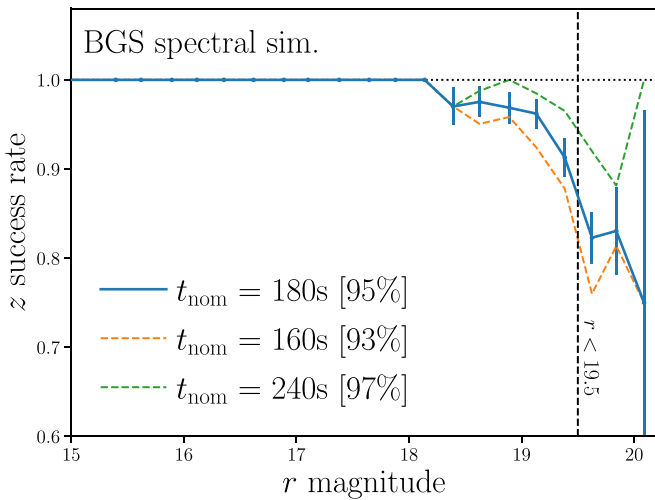
Figure 5. Redshift success rate of spectral simulations run using a nominal exposure time of $t_{nom} = 180$ s (blue) as a function of r-band magnitude. We include z success rates for spectral simulations run using $t_{nom} = 160$ (orange dashed) and 240 s (green dashed) for comparison. The overall z success rates of all $r < 19.5$ galaxies are presented in the legend. These simulations assume spectra based on realistic continuum templates derived from AGES, matched to g, r, z LS photometry, and GAMA emission-line fluxes. They incorporate realistic noise and throughput for BGS observations. With $t_{nom} = 180$ s, we predict that the BGS Bright sample can achieve an overall redshift success rate of 95%.

response, characterized by gain, dark current, and readout noise, is simulated to produce realistic DESI-like spectra.

Next, we measure redshifts of the simulated BGS spectra using REDROCK,[59] the redshift fitter for DESI (S. Bailey et al. 2023, in preparation). REDROCK finds the best-fit redshift using χ^2 minimization computed from a linear combination of principal component analysis (PCA) basis spectral templates. REDROCK separately determines the redshift that minimizes the χ^2 for three template classes ("stellar," "galaxy," and "quasar") over their specific redshift range. Afterward, the redshift and spectral class that give the lowest χ^2 value is considered the best description of the spectrum. REDROCK also provides a redshift confidence, $\Delta\chi^2$, based on the difference between the χ^2 values of the best-fit REDROCK model and the next best-fit model. We consider a BGS redshift as successful if (1) no warning flags, e.g., for poor fits or bad data, are raised; (2) $\Delta\chi^2 > 40$ (Section 5.3); and, in this case, (3) the measured redshift, z', closely reproduces the true redshift z_{true} of the simulation, $|z' - z_{true}|/(1 + z_{true}) < 0.0033 \simeq 1000$ km s^{-1}.

In Figure 5, we present the redshift success rate as a function of r magnitude for spectral simulations run using exposures times of $t_{exp} = 180$ (blue), 160 (orange), and 240 s (green). We include Poisson uncertainties of the redshift success rate, for reference. We mark the $r < 19.5$ mag limit of the BGS Bright sample (black dashed) and the overall redshift success rate of all $r < 19.5$ galaxies in the legend. Based on the spectral simulations, we predict that we can achieve an overall redshift success rate of ~95% for a sample limited to $r < 19.5$ with the nominal BGS exposure time of $t_{nom} = 180$ s. Every BGS exposure time will be scaled based on this 180 s nominal exposure time and its individual observing conditions to achieve uniform redshift efficiency. For details on how BGS exposure times are set during observations, we refer the reader to E. Schlafly et al. (2023, in preparation).

4.2. Observing Strategy

During bright conditions, DESI will observe the bright-time programs: BGS and MWS. The decision on whether to observe the dark- or bright-time programs is determined by a threshold on "survey speed," which is a diagnostic based on observing conditions, such as seeing, transparency, air mass, and sky brightness. BGS will aim to cover 14,000 deg^2 with a footprint that closely matches the dark program. The footprint will be covered by 5675 "tiles," which are planned DESI pointings, that are arranged according to a nonoverlapping "best packing" scheme. The scheme requires tiles in a single pass to have a minimum separation of 3°.411. BGS will be observed with four passes such that each point in the footprint will be visited three times on average, to satisfy the requirement that 80% of targets are observed spectroscopically.

To assess the feasibility of the BGS strategy above, we use survey simulations to forecast the progress of the DESI survey. The survey simulations, as described in detail in D. Schlafly et al. (2023, in preparation), simulate the nightly operations of DESI as a sequence of tile exposures.[60] They account for the expected configuration and dead time of both the telescope and instrument and assume historical weather and environmental factors appropriate for Kitt Peak. Lunar conditions, which are defined by tabulated ephemerides, play a key role in the simulation. The simulated exposure time is scaled according to the predicted sky brightness relative to nominal conditions at the time of observation for the tile, which will depend on the lunar phase and position. We use an empirical sky background model derived from SV exposures and the nominal exposure time defined in Section 4.1. We describe the sky model in detail in Appendix B.

In Figure 6, we present the survey footprint observed over the 5 yr operation of DESI, as predicted by survey simulations. Each panel shows the BGS tiles that are completed up to and including that year. We plot the ecliptic for reference (black dotted). We assume a lunar exclusion zone of radius 50°, which is apparent in the reduced coverage close to the ecliptic in early years. Based on the survey simulation, the effective three-visit coverage is achieved for the 14,000 deg^2 footprint after 4 yr, which leaves 20% of the total DESI operation time as margin.

4.3. Fiber Assignment Strategy

The focal plane of DESI contains 5000 fibers arranged in 10 wedge-shaped petals. Each fiber is controlled by a robotic fiber positioner, which can rotate on two arms and be positioned within a circular patrol region of radius 1′.48 (DESI Collaboration et al. 2016a, 2022; Schubnell et al. 2016; Silber et al. 2023). The patrol regions of adjacent positioners slightly overlap; however, there are gaps in the regions between the petals. For each tile we dedicate a minimum of 40 "sky" fibers per petal to measure the sky background for accurate sky subtraction. An additional 10 fibers per petal are assigned to standard stars for flux calibration (Guy et al. 2023). The rest of the "science" fibers are assigned to BGS targets on each tile according to the following fiber assignment strategy (Raichoor et al. 2023).

First, we assign a primary priority to BGS targets. Our first goal is to obtain a magnitude-limited BGS Bright sample that is as complete as possible to simplify clustering analyses. So we

59 https://redrock.readthedocs.io

60 https://surveysim.readthedocs.io/
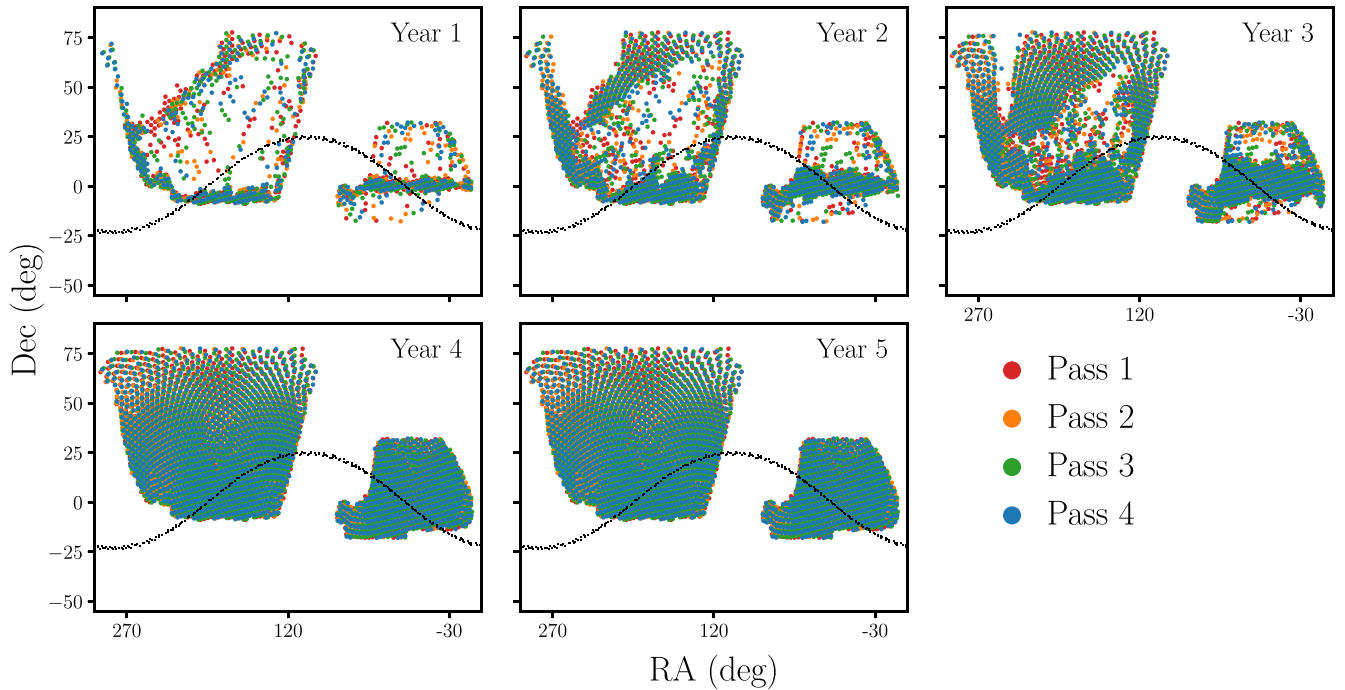
Figure 6. BGS tiles observed by DESI over its 5 yr of operation according to survey simulations. In each panel, we present BGS tiles that will be observed up to and including that year. BGS will observe a footprint of 14,000 deg^2, which will match the footprint of the dark program as closely as possible, with a four-pass strategy. Each point on the footprint will be visited three times on average. For reference, we mark the ecliptic in each panel (black dotted). According to survey simulations, we achieve the 14,000 deg^2 footprint with four passes after 4 yr and meet the required 20% operational survey margins.

assign the highest priority to BGS Bright targets. Next, we assign lower priorities to 80% of the BGS Faint targets.[61] If we were to assign lower priorities to all BGS Faint targets, measurements of clustering in the BGS Faint sample would suffer significantly from uncertain fiber assignment incompleteness corrections. For instance, in regions with a high density of BGS Bright targets, BGS Faint targets would not be assigned to fibers (Smith et al. 2019). This would lead to certain galaxy pairs having zero probability of assignment, which would be impossible to correct in later clustering analyses (e.g., Hahn et al. 2017; Bianchi et al. 2018). To reduce this effect and to facilitate corrections for fiber assignment incompleteness, we randomly promote 20% of BGS Faint targets to the same priority as BGS Bright.[62] Lastly, the BGS AGN targets are assigned at the same priority as BGS Faint. BGS shares the focal plane with the MWS, whose targets enter at a lower priority than both BGS Faint and BGS AGN targets.

After the primary priorities are assigned, a uniform random subpriority in the range (0, 1) is generated for each object. The total priority is the sum of the primary and subpriority values. Fibers are assigned to targets in their patrol region in rank order of total priority. With this strategy, fiber assignments to targets with the same primary priority are randomized, but a higher primary priority target will always be assigned a fiber in preference to a lower primary priority target. We note that targets with higher priority than BGS Bright are rare and are typically standard stars or MWS white dwarfs. In addition, the lowest-priority targets are occasionally "bumped" on a tile-by-tile basis to satisfy the sky fiber requirement. Occasionally,

targets whose redshifts were unsuccessfully measured are reobserved but reassigned lower priority (see Raichoor et al. 2023 for details). In Section 5.4, we present the fiber efficiencies that result from this strategy for each of the BGS target types.

5. Survey Validation

Before beginning its 5 yr of operations, DESI conducted the SV campaign with the primary goal of verifying that the main survey will meet its requirements. In this section, we use SV observations to validate the BGS selection cuts (Section 3) and demonstrate that BGS will meet the requirements we set to ensure that it will achieve its broad range of science goals. The requirements include stellar contamination rates less than 1%, redshift efficiency above 95%, and fiber assignment efficiency above 80%. In Section 5.1, we describe the SV observations in further detail. We then use these observations to validate the selection cuts (Section 5.2), redshift efficiency (Section 5.3), and fiber assignment efficiencies (Section 5.4).

5.1. SV Observations

The SV campaign was divided into two main phases: the first, SV1, observed fields spanning the expected footprint and aimed to characterize performance for different observing conditions and optimize sample selection. The second program, the One-Percent Survey, aimed to observe a data set that can be used for representative clustering measurements and deliver a "truth" sample with high completeness ($\gtrsim$99% for BGS Bright) over an area at least 1% of the expected main survey footprint. We use the One-Percent Survey data to predict the redshift efficiency for BGS targets in the main survey. In the following, we describe the characteristics of the SV1 and One-Percent

---

[61] The numerical values of these priorities are 2100 for the highest priority and 2000 for the lower priority.
[62] In the DESI catalogs these BGS Faint targets with higher priority are labeled under the BGS_FAINT_HIP bit name.

Survey programs in further detail and explain the relevance for the tests performed in this work.

SV1 observed on 76 nights over ∼5 months from 2020 December to 2021 April. During this time, we observed 562 bright-time exposures that cover 50 unique BGS tiles with an effective area 310 deg^2. In Figure 1, we mark the BGS tiles observed during SV1 in red. The tiles span the expected DESI footprint and cover both the NGC and SGC. They also cover imaging from both DECaLS and BASS+MzLS. Some targeted regions where the imaging surveys overlap to investigate differences in target selection due to the differing imaging quality and photometric systems. Additional tiles were chosen to overlap with external surveys, e.g., the GAMA G02 and G12 fields, in order to compare redshifts from them to those from DESI. Tiles were also chosen to include regions with challenging imaging conditions, including strong dust extinction and high stellar density near the Galactic plane. Furthermore, SV1 targets were chosen with a broader selection to determine the selection that performs best in those conditions. We describe the full SV1 selection in Appendix A.

In addition to their positions, SV1 exposures were observed at different times to span a broad range of observing conditions (air mass, Galactic extinction, transparency, and seeing). Moreover, the exposures were observed during times with widely varying sky brightness: 17–24 mag based on both the Guide Focus Array cameras (GFA; DESI Collaboration et al. 2016b) and sky spectra. Exposures were taken during nearly all lunar conditions spanning different combinations of Moon illumination, altitude, and separation. Each SV1 field was required to have one dark exposure. The remaining exposures were taken with ∼300 s exposure times on different nights such that they were observed over a range of conditions and hour angles. We compile "cumulative" coadds of all exposures of a given tile to date to serve as deeper "truth tables."

Shortly after the SV1 program, the SV2 program dedicated a short amount of available time to developing main survey operations. The One-Percent Survey (or SV3) then observed on 38 nights from 2021 April to the end of 2021 May. During this time, we observed 288 bright-time exposures that cover 214 BGS tiles. The One-Percent Survey was designed to operate similarly to the main DESI survey but at much higher completeness. One-Percent Survey pointings, therefore, targeted sets of 11 overlapping tiles with centers arranged around a 0°.12 circle, forming a "rosette" completeness pattern. In total, the One-Percent Survey observed 20 rosettes that cover an area of 180 deg^2, of which 140 deg^2 was of the desired completeness for BGS Bright. The rosettes spanned the NGC footprint and several were chosen to overlap with external surveys, including GAMA, DEEP2, AGES, and HSC. In Figure 1, we mark the One-Percent Survey tiles on the DESI footprint in orange.

Although the One-Percent Survey exposures were not observed in widely varying observing conditions, they are nevertheless representative of conditions expected during bright time. Unlike the SV1 exposures, t_{exp} were set by the ETC, as in the main survey. The ETC dynamically scaled the $t_{nom} = 180$ s nominal exposure time according to observing conditions (Section 4.1). For long observation sequences, the ETC also decided how the observation is split into multiple exposures. To achieve a very high spectroscopic completeness, exposure times were 20% longer than that expected of the main

survey. The total exposure times for the One-Percent Survey range between 220 and 2670 s, with a median exposure time of 480 s. Targets with failed redshifts were reobserved at lower priority. A target could be reobserved up to nine times if we continued to fail in measuring its redshift (see Myers et al. 2023 for details). The longer exposure time and reassignment of targets allowed for the construction of accurate redshift "truth tables" at greater depth for the vast majority of One-Percent Survey targets. The ETC was also continuously updated and calibrated throughout One-Percent Survey. Hence, the exposure times are more variable than what we expect for the main survey. We refer readers to DESI Collaboration et al. (2023, in preparation) for further details on the SV programs.

After the SV programs, the main survey began on 2021 May 14 and proceeded until the seasonal Arizona monsoon in July prevented observations for a number of months. The 343 main survey tiles observed over the first ∼2 months delivered 532,796 BGS redshifts. Some of the later tests we present in this work include observations from this period to further ensure that we meet the stated requirements for the final survey design choices.

All BGS targets observed during SV1 and the One-Percent Survey are reduced using the spectroscopic data reduction pipeline. Briefly, spectra are first extracted from the spectrograph CCDs using the *Spectro-Perfectionism* algorithm (Bolton & Schlegel 2010). Then, fiber-to-fiber variations are corrected by flat-fielding, and a sky model, derived from the (at least 400) sky fibers, is subtracted from each spectrum. Afterward, fluxes are calibrated using stellar model fits to standard stars. The calibrated spectra are then co-added across exposures of the same tile to produce the final processed spectra with an effective exposure time equal to t_{nom}. The full spectroscopic data reduction is described in Guy et al. (2023). We present a few examples of BGS spectra selected from the One-Percent Survey observations in Figure 7.

5.2. Validating Selection Cuts

To construct BGS Bright and Faint samples appropriate for science, we apply spatial masking, star–galaxy separation, FMC, quality cut, and bright limit to potential targets (Section 3.1). We validate each of these selections using SV data in the following.

First, we validate the spatial masking around bright stars by examining the number density of BGS targets inside and outside the masks. We compare the density of BGS objects with the mean density as a function of angular separation from the bright star as in Ruiz-Macias et al. (2021). Within the spatial masking radius, R_{BS}, the target density is significantly lower than the mean density. This is because TRACTOR fits objects near bright stars with a PSF model, so they are often excluded from the target catalog by the BGS selection cuts. On the other hand, outside R_{BS}, we find that the BGS target density is in good agreement with the mean density. This confirms that excluding the regions within our bright star masks sufficiently accounts for the impact of bright stars.

Next, we validate our star–galaxy separation criteria using SV1 observations, where we imposed a more relaxed star–galaxy separation (Appendix A). In SV1, in addition to objects that pass our star–galaxy separation, we also select objects below the $(G_{Gaia} - r_{raw}) = 0.6$ threshold that are not classified as PSF by TRACTOR. In the middle panel of Figure 2, we present the stellar contamination fraction of BGS objects in
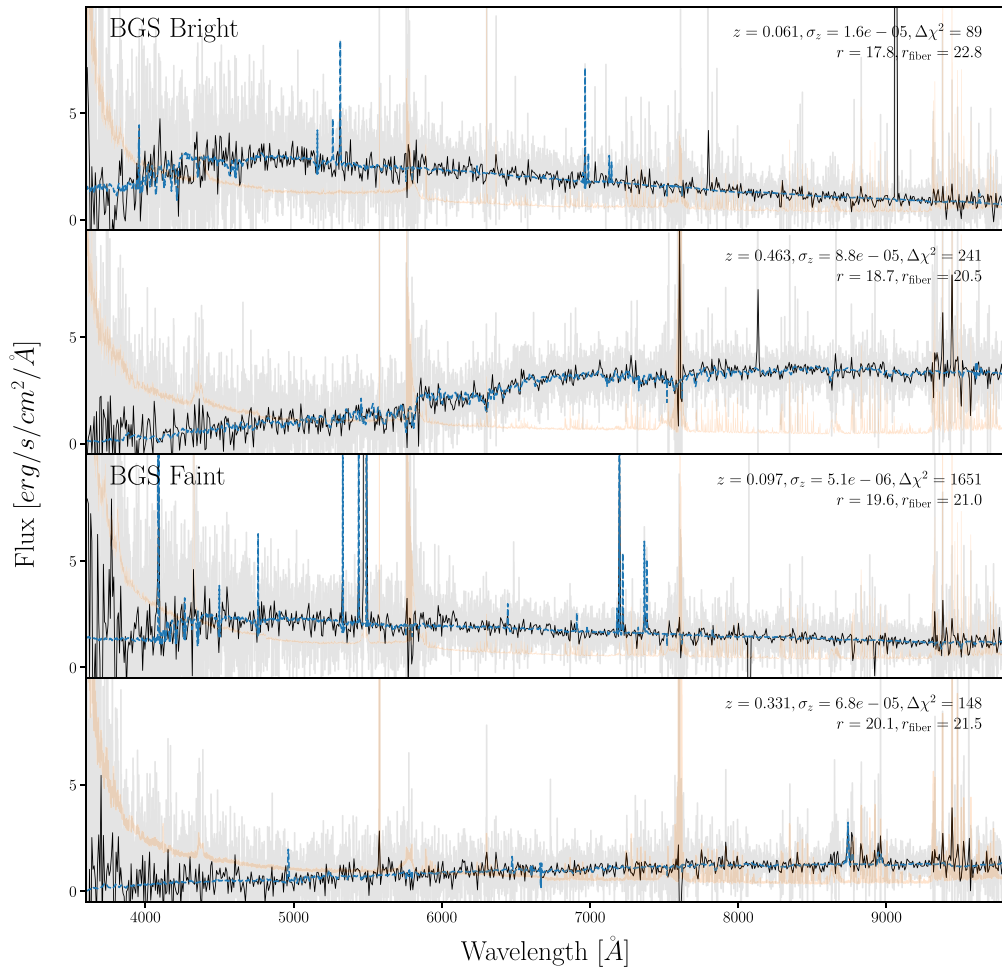
Figure 7. BGS galaxy spectra from the One-Percent Survey (gray). We present spectra of a blue and a red galaxy from the BGS Bright sample and a blue and a red galaxy from the BGS Faint samples (top to bottom panels). In each panel, we also plot the spectrum rebinned to a coarser wavelength grid (black) and the measured uncertainties (orange), and we include the best-fit REDROCK template used to measure the redshift (blue). The redshift measurement, uncertainty, and $\Delta\chi^2$ from REDROCK are included in the upper right corner, along with the r-band magnitude and fiber magnitude of the galaxy.

SV1. Stellar contamination is determined using DESI spectra based on spectral classification by REDROCK and a $z < 300$ km s^{-1} redshift limit. We represent the contamination rate in hexbins using the color mapping. We only include bins with more than 10 galaxies to ensure accurate estimates. Below the $(G_{\rm Gaia} - r_{\rm raw}) = 0.6$ threshold, we find significant stellar contamination; some of the bins have >20% stellar contamination. In contrast, we find low stellar contamination rates above the threshold. The low stellar contamination rate is further confirmed by the right panel of Figure 2, where we present the stellar contamination fraction of BGS objects in the One-Percent Survey. The One-Percent Survey only includes objects that pass our star–galaxy separation. We find <1% stellar contamination throughout the entire sample. We also find no significant difference in the stellar contamination rate near the Galactic plane.

For the FMCs, the bounds of the cuts are already determined by visual inspection and by comparison to GAMA redshifts of matched galaxies. We further confirm, spectroscopically, that the BGS targets in SV1 observations that fail these cuts are not galaxies and have low redshift efficiencies. Next, to test the quality cuts proposed in Ruiz-Macias et al. (2021), we use 2000 BGS targets spread across a 420 deg^2 area of DECaLS that were visually inspected. By visual inspection, we confirm that

TRACTOR-based quality cuts discussed in Ruiz-Macias et al. (2021) remove a significant number of real galaxies in DR9. Removing these quality cuts increases the BGS target completeness without introducing a significant number of spurious objects (see also Zarrouk et al. 2021). We similarly validate the bright limit using visual inspection and confirm that most of the sources excluded by the cut are not galaxies—nearly all are saturated stars.

In addition to validating the selection cuts that we impose, we further examine whether any imaging property systematically impacts the BGS target density. In Figure 8, we examine whether stellar density; galactic extinction; PSF size in g, r, z bands; or photometric depth in g, r, z, $W1$, $W2$ bands impact the target densities, η, of the BGS Bright (blue) and Faint (orange) samples. The target densities are measured in HEALPIX[63] pixels with resolution of $N_{\rm side} = 256$ (equivalent to an area of 0.05 deg^2). We divide η by the average target density of the samples over the 14,000 deg^2 DESI footprint, $\bar{\eta}$, to highlight any variations or dependencies. Here $\bar{\eta} = 864$ and 533 targets deg^{-2} for the BGS Bright and Faint samples, respectively. In each panel, we also represent the distribution of the imaging property with a normalized histogram. Stellar

---

[63] http://healpix.sourceforge.net (Górski et al. 2005)
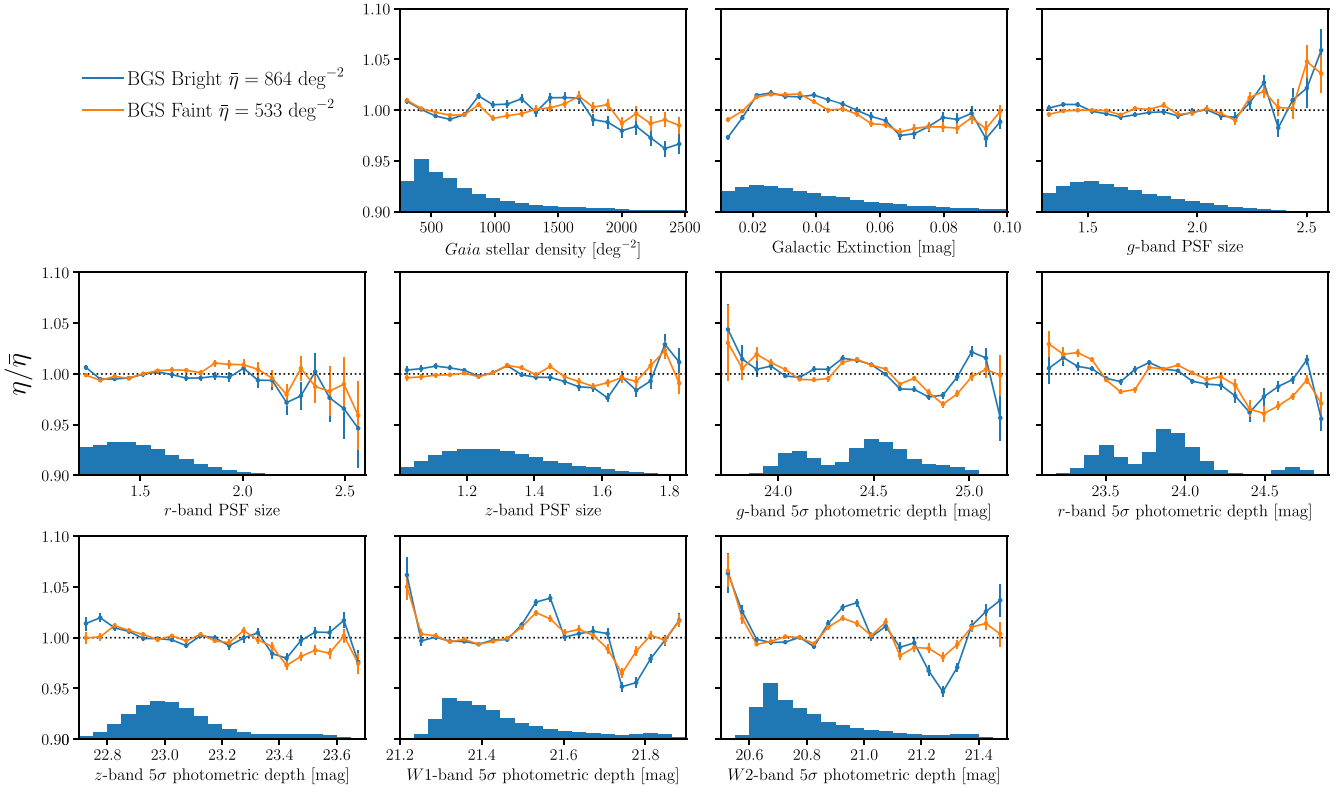
Figure 8. The dependence of BGS Bright (blue) and Faint (orange) target densities on different imaging properties: stellar density, galactic extinction, PSF size (in g, r, and z bands), and photometric depth (in g, r, z, $W1$, and $W2$ bands). The target densities, η, are divided by the average target density of the samples over the 14,000 deg^2 DESI footprint ($\bar{\eta}$; included in the legend) to highlight variations. The error bars represent the uncertainties on the mean. The histogram in each panel represents the normalized distribution of each imaging property. We find the consistency of Bright and Faint target densities especially encouraging because we use more complex cuts in the latter. Overall, we find $<5\%$ variation in the target densities of BGS Bright and Faint samples and no strong systematic dependence on imaging properties.

density is measured using Gaia DR2 stars with $12 < G_{\rm Gaia} < 17$. Galactic extinction is measured using SFD98 dust maps (Section 2.1). PSF size denotes the FWHM in arcseconds. Photometric depth is characterized by the 5σ AB magnitude detection limit for a $0\rlap.{''}45$ round exponential galaxy profile.

Overall, we find $<5\%$ variation in the target densities of both BGS Bright and Faint samples. These variations are significantly lower than for the preliminary BGS target selection described by Ruiz-Macias et al. (2021). We find no evidence for significant stellar contamination, which would increase the target density in high stellar density regions. The target density is slightly lower for regions with stellar density >2000 deg^{-2}; however, the relative area is small. In principle, this effect could be due to photometry being impacted for sources near bright stars outside our bright star spatial masking. However, we rule out this possibility because we find little change in $(\eta/\bar{\eta})$ even when the spatial masking is extended significantly. We also find slightly lower target densities in regions with high dust extinction, which spatially correlates with stellar density. A more detailed investigation of the correlation of BGS target densities with stellar density and dust extinction is necessary. Clustering analyses will likely require systematic weights derived using linear regression or machine-learning techniques to mitigate the effect of any spatial correlations (e.g., Rezaie et al. 2020; Ruiz-Macias et al. 2021). We find no strong dependence in the target densities for the PSF size or photometric depth in any of the photometric bands, and we find the agreement of BGS Bright and Faint to be encouraging,

given the more complex selection of the latter. Overall, the variations in target densities seem consistent with random fluctuations from large-scale structure; however, further investigation with simulations and observation is necessary.

5.3. Redshift Efficiency

One of the main goals of SV is to validate the BGS redshift efficiency for the main survey. We seek to verify that we can achieve our desired 95% redshift efficiency with the 180 s nominal exposure time (Section 4) under BGS conditions. Out of the 562 SV1 and 288 One-Percent Survey BGS exposures, we focus on spectra collected from exposures with effective exposure times close to 180 s, the effective exposure time expected in the main survey. In practice, we use exposures with 160 s $<$BGS_EFFTIME_BRIGHT< 200 s, where BGS_EFF-TIME_BRIGHT is our best spectroscopically derived estimate of the effective exposure time achieved for BGS targets. It takes into account the transparency measured from standard stars together with ETC-derived fiber losses and sky background.

We measure redshifts for all the spectra from the selected SV exposures using REDROCK, as we did for the spectral simulations in Section 4. However, unlike the spectral simulations, we do not know the true redshifts. Instead, we use the "deep" coadds constructed from the SV1 and One-Percent Survey exposures as our redshift "truth table" (Section 5.1). We exclude spectra from SV exposures that do not have deep redshifts because we do not know their "true" redshifts. We further exclude spectra that have corresponding
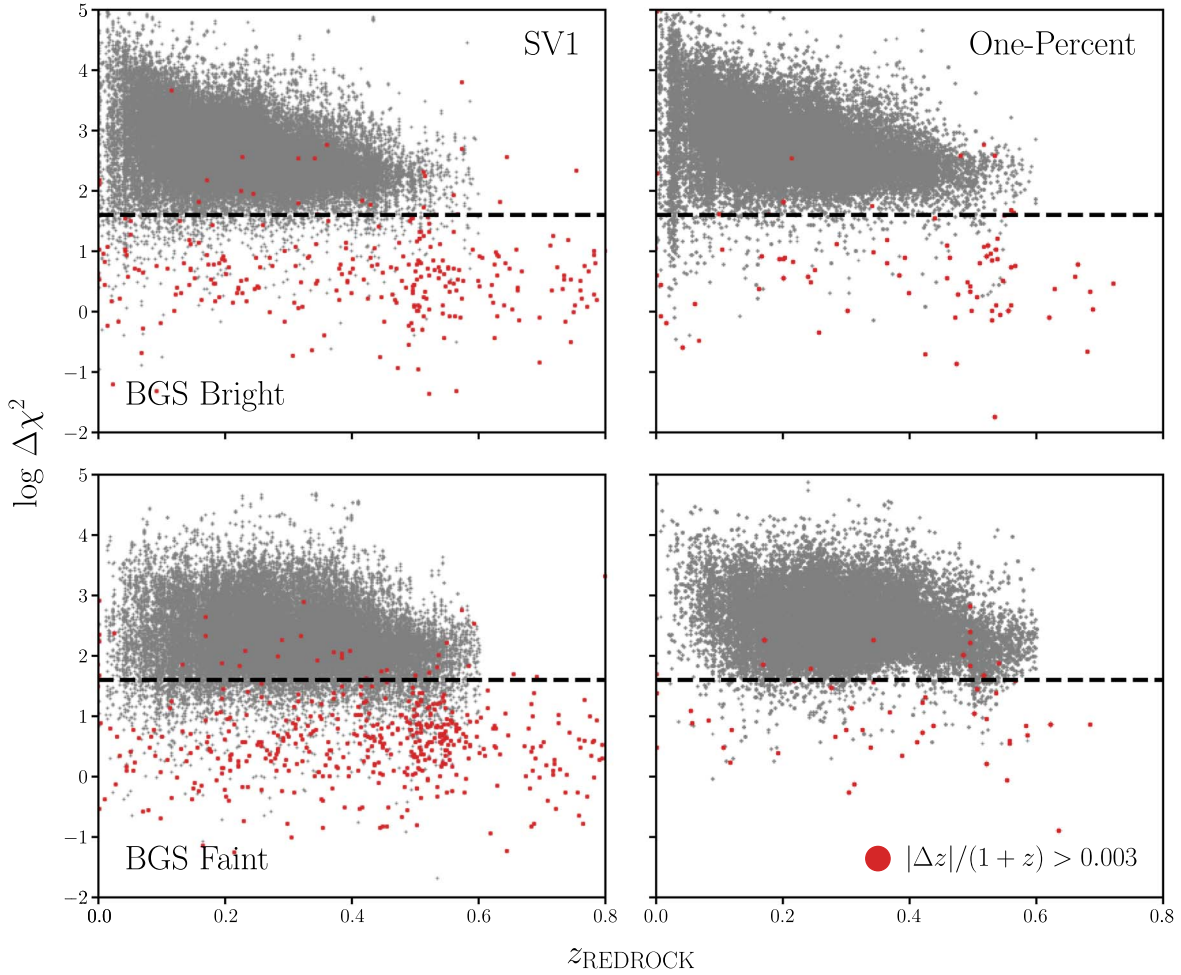
Figure 9. REDROCK $\Delta\chi^2$ as a function of best-fit redshift, z_{Redrock}, for BGS Bright (top) and Faint (bottom) galaxies from the SV1 (left) and One-Percent Survey. $\Delta\chi^2$ and z_{Redrock} are measured using spectra from single BGS-like exposures. We highlight the spectra that have catastrophic redshift discrepancies with the redshift measured from corresponding deep exposures, $|\Delta z|/(1+z) > 0.0033$, in red. Our $\Delta\chi^2 > 40$ criterion for redshift success (black dashed) excludes the majority of catastrophic redshift failures. Conversely, below the $\Delta\chi^2$ threshold, ~30% and ~15% of BGS Bright and Faint galaxies, respectively, have catastrophic redshift failures.

deep coadds with individual exposure times <2000 s for SV1 and `BGS_EFFTIME_BRIGHT` < 100 s for the One-Percent Survey. This is to ensure that our "true" redshifts are derived from spectra with sufficient depth. We also exclude spectra where there were any known issues with the fiber assignment. Furthermore, for the One-Percent Survey, we exclude spectra that required more than one observation to determine a valid redshift. These are spectra of targets that have failed initial redshifts, so they may bias our redshift efficiency estimates. For some of the spectra, REDROCK classifies their corresponding deep spectra as stellar or measures a redshift outside the $0 < z < 0.6$ BGS range. We consider these cases as failures in targeting and thus exclude them when estimating redshift efficiency.

From the remaining spectra (125,472 in SV1 and 176,688 in One-Percent Survey), we classify a REDROCK redshift as a success if the following criteria are met:

1. no REDROCK warning flags are raised;
2. the best-fit REDROCK SPECTYPE is "galaxy";
3. the reported redshift error is small relative to the measured redshift, ZERR $< 0.0005(1+z)$;

4. the redshift confidence—as judged by the difference in χ^2 between the two best-fitting models—is significant: $\Delta\chi^2 > 40$;
5. z_{deep} is reliable—i.e., the deep spectrum meets criteria 1, 3, and 4;
6. z is consistent with the corresponding z_{deep} at 1000 km s^{-1}: $|z_{\mathrm{deep}} - z|/(1 + z_{\mathrm{deep}}) < 0.0033$.

The specific limits in criteria 3 and 6 are BGS requirements that we set on the statistical error (<150 km s^{-1}) and catastrophic redshift failures.

We choose the $\Delta\chi^2 > 40$ threshold in criterion 4 to exclude the majority of catastrophic redshift failures. In Figure 9, we present $\Delta\chi^2$ as a function of measured redshift z_{Redrock} for the BGS Bright (top) and Faint (bottom) samples in SV1 (left) and the One-Percent Survey (right). We mark spectra that fail criterion 6 (catastrophic redshift failures) in red. The $\Delta\chi^2 > 40$ threshold (black dashed) removes the majority of spectra with catastrophic failures for all of the samples. Conversely, below the threshold, ~40% of BGS Bright galaxies and ~25% of BGS Faint galaxies are redshift failures, making this regime unreliable for statistical or clustering studies. Furthermore, in
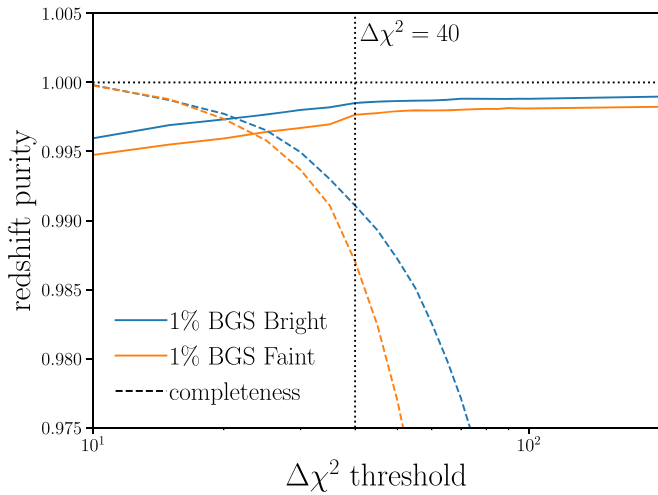
Figure 10. Redshift purity (solid) as a function of the REDROCK $\Delta\chi^2$ threshold for the redshift success definition of the BGS Bright (blue) and Faint (orange) samples. We also present the redshift completeness, the fraction of successful redshifts included for a given $\Delta\chi^2$ threshold. We assess redshift success according to the criteria listed in Section 5.3 based on redshifts measured from corresponding deep exposures. The $\Delta\chi^2 > 40$ threshold we impose to determine redshift success results in a BGS Bright sample with $>99.5\%$ purity and $>99\%$ completeness.

Figure 10, we present overall redshift purity as a function of the $\Delta\chi^2$ threshold limit for the BGS Bright (blue) and Faint (orange) samples. Redshift purity corresponds to the fraction of gray points that lie above the dashed line in Figure 9. For reference, we also include the redshift completeness as a function of the $\Delta\chi^2$ threshold. The completeness here is the fraction of the total "accurate" redshifts included in the $\Delta\chi^2$ threshold. We consider a REDROCK redshift as "accurate" if it passes criteria 1, 2, 3, 5, and 6 above. A similar calculation of purity and completeness using select galaxies with visually inspected redshifts produces consistent values (Lan et al. 2023; Figure 7). Given the choice of $t_{nom} = 180$ s, our $\Delta\chi^2 > 40$ threshold provides a BGS Bright sample with $>99.5\%$ purity and $>99\%$ completeness, as well as a BGS Faint sample with $>99.5\%$ purity and $>98.5\%$ completeness.

In Figure 11, we present the redshift success rate as a function of r-band magnitude for BGS galaxies from the One-Percent Survey observations (blue). We also include the redshift success rate of BGS galaxies from SV1 observations (green dashed), excluding those in the *Low Quality* class (Appendix A). We remind readers that the BGS galaxies, especially the faint $r > 19.5$ galaxies, in the SV1 observations are more broadly selected than those in the One-Percent Survey (see Section 5.1 for details). We represent the Poisson uncertainties of each magnitude bin with the error bars. Focusing first on the $r < 19.5$ BGS Bright sample, Figure 11 demonstrates that we achieve $>95\%$ redshift success rate for $r < 19.5$. Furthermore, we find little magnitude dependence on the redshift success rate throughout the $r < 19.5$ mag range. Hence, the SV observations clearly demonstrate that the BGS Bright sample can achieve the $>95\%$ redshift efficiency requirement with the 180 s nominal exposure time.

We further examine the redshift success rate in Figure 12, as a function of r and r_{fiber} magnitudes for the SV1 (left) and One-Percent Survey (right). The color map represents the redshift success rate. For SV1, we again exclude the spectra in the *Low Quality* class. To highlight the desired 95% threshold, we present the bins with $>95\%$ redshift success rates with a blue color
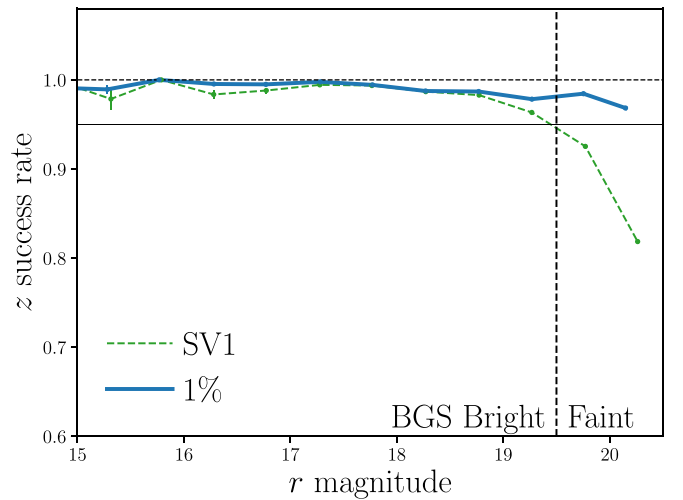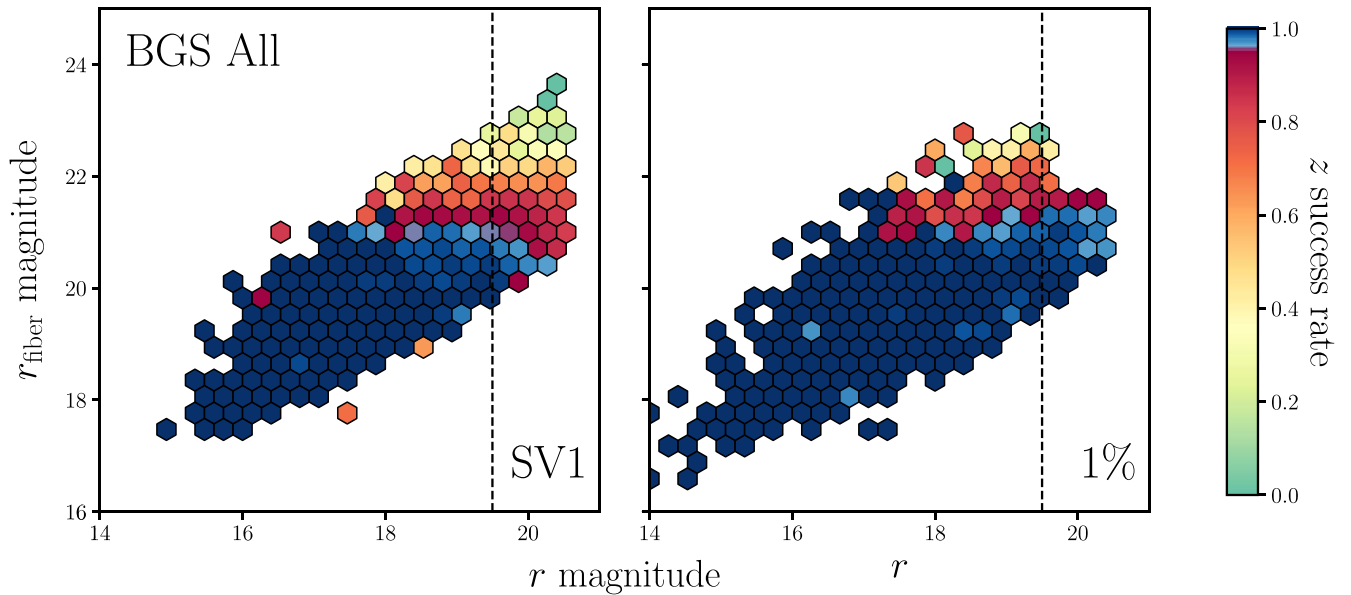

Figure 11. Redshift success rate as a function of r-band magnitude for galaxies in the One-Percent Survey observations (blue). The z success rates are estimated using the criteria listed in Section 5.3 and only include spectra from exposures that correspond to $t_{nom} \sim 180$ s. The error bars represent the Poisson uncertainties for each magnitude bin. We mark the $r = 19.5$ mag cut that separates the BGS Bright and Faint samples (black dashed). We include the z success rate for SV1 galaxies, excluding the *Low Quality* class, for reference. BGS galaxies in SV1 are more broadly selected than in the final target selection. We achieve z success rate $>95\%$ for the entire BGS sample throughout its full r magnitude range. We achieve overall z success rates of 98.4% and 97.9% for BGS Bright and Faint, respectively, in the One-Percent Survey.

mapping. The remainder are shown with an independent color bar of greater range. We only include bins with more than 10 galaxies to ensure accurate estimates. Consistent with Figure 11, we find mostly $>95\%$ redshift success rate for the BGS Bright sample (left of the black dashed line). We note that some of the bins with $r_{fiber} > 21.5$ do not meet the 95% threshold. This is more apparent for the SV1 sample, which has a more relaxed separation cut (Appendix A). For the final selection, even at $r_{fiber} > 21.5$, the redshift success rate remains $>90\%$.

We also examine the redshift success rate of the BGS Bright sample as a function of $g - r$ and $r - z$ color in Figure 13. Again, we present the success rates for the SV1 and One-Percent Survey in the left and right panels, respectively. We split the sample by the median redshift of the BGS Bright sample: $0.0 < z < 0.2$ galaxies (top panels) and $0.2 < z < 0.6$ galaxies (bottom panels). The color map represents the redshift success rate, and we use a blue color map for the bins with $>95\%$ redshift success rate. We exclude bins with less than 10 galaxies. We mark the 68th and 95th percentile contours of the color distribution of the One-Percent Survey BGS Bright galaxies in the right panels for reference (white dashed). Galaxies in the BGS Bright sample form a tight locus in color space, well within the color cuts we impose in the quality selection cuts (Equation (4)). Moreover, we find no strong color dependence in the redshift success rate. The slightly lower redshift success rate in the bluest galaxies with $g - r < 0.4$ is primarily driven by their overall fainter magnitudes. Only a small fraction of BGS Bright targets lie in regions of lower redshift success rate (top right). Overall, we find $>90\%$ redshift success rate throughout the galaxy color space for the One-Percent Survey.

Next, we focus on the BGS Faint sample. In Figure 11, the One-Percent Survey observations demonstrate that we meet the $>95\%$ redshift success rate for the BGS Faint sample over its

Figure 12. Redshift success rate of BGS galaxies as a function of r and $r_{\rm fiber}$ magnitudes. We present BGS spectra from SV1 (left) and the One-Percent Survey (right). The color map represents the z success rate; hexbins with >95% redshift success rate are marked with a blue color mapping. For the BGS Bright sample, we find overall >95% redshift success rates. Galaxies with fainter $r_{\rm fiber}$ > 21.5 have lower redshift success rates, as expected. However, even for the small fraction of galaxies with $r_{\rm fiber}$ > 21.5, BGS Bright maintains a $\gtrsim$90% redshift success rate with the final selection (right). For the BGS Faint sample, the $r_{\rm fiber}$−color cut in the One-Percent Survey selection excludes galaxies with the lowest redshift success rates in SV1. As a result, the BGS Faint sample has high redshift success rates (>90%) throughout its entire r−$r_{\rm fiber}$ range.

entire r magnitude range. We also note that the redshift rate of the BGS Faint sample in the One-Percent Survey is significantly higher than in the SV1 observations. This is driven by the $r_{\rm fiber}$−color cut used in the One-Percent Survey, which is not used in the SV1 BGS Faint selection. As Figure 12 demonstrates, the $r_{\rm fiber}$−color cut excludes faint $r_{\rm fiber}$ > 21.5 galaxies with low redshift success rate and significantly increases the redshift success rate for the BGS Faint sample. With the $r_{\rm fiber}$−color cut, even at the $r_{\rm fiber}$ ∼ 21.5 limit, we maintain >87% redshift success rate.

We further illustrate the effectiveness of the $r_{\rm fiber}$−color BGS Faint selection in Figure 14. We present the redshift success rate of the BGS Faint sample as a function of $r_{\rm fiber}$ and $(z - W1) - 1.2(g - r) + 1.2$ color. The color map represents the redshift success rates, and we mark the $r_{\rm fib}$−color cut (black dashed). SV1 BGS Faint objects outside the $r_{\rm fiber}$−color cut have significantly lower redshift success rates. Meanwhile, SV1 BGS Faint objects within the $r_{\rm fiber}$−color cut and the One-Percent Survey BGS Faint objects have >90% redshift success rates. The $(z - W1) - 1.2(g - r) + 1.2$ color is a proxy for emission-line strengths (e.g., Hα and Hβ). Therefore, the $r_{\rm fiber}$−color cut successfully removes objects with low redshift efficiency, and by selecting on this cut, we achieve a >95% redshift success rate for the BGS Faint sample.

BGS will be observed under bright-time conditions. In practice, observing conditions are classified as bright or dark time based on the survey speed metric (D. Schlafly et al. 2023, in preparation). Survey speed assesses the rate at which S/N increases for a fiducial target for a given observing condition. In clouded-out conditions, survey speed is 0; in the best conditions, survey speed is ∼2.5. When survey speed is within a nominal range of $[\frac{1}{6}, 0.4]$, DESI will observe the bright-time programs (BGS and MWS). Above this range, DESI observes the dark-time programs, and below it a "BACKUP" program of particularly bright stars. Survey speed boundaries may be

adjusted during the main survey to ensure that the dark and bright surveys proceed at the planned rate. In Figure 15, we examine whether the redshift success rate of BGS galaxies has any significant dependence on survey speed. We present redshift success rate of all BGS galaxies in the One-Percent Survey (blue) and main survey (orange), as well as BGS Bright galaxies in SV1 (green). Throughout the BGS survey speed range, we find little dependence on survey speed. Moreover, we achieve a >95% redshift success rate throughout the bright-time observing conditions.

In addition to the internal assessments, we can also compare BGS redshift measurements to previous spectroscopic surveys because SV exposures were observed in multiple overlapping regions (Section 5.1). The GAMA survey DR4 (Driver et al. 2022), with its comparable magnitude-limited selection, provides an ideal sample for assessing BGS redshifts. The GAMA sample extends to $r_{\rm SDSS}$ < 19.8, where $r_{\rm SDSS}$ is the SDSS r-band Petrosian magnitude. In total, ∼25,000 BGS galaxies in the SV1, One-Percent Survey, and main survey were observed by GAMA and have high-quality redshifts (NQ > 2). In Figure 16, we compare the BGS redshifts, $z_{\rm BGS}$, to GAMA redshifts, $z_{\rm GAMA}$, for these overlapping galaxies from the SV1 (green), One-Percent Survey (blue), and main survey (orange). The top panel shows $z_{\rm GAMA}$ as a function of $z_{\rm BGS}$, with $z_{\rm GAMA} = z_{\rm BGS}$ included for reference (black dashed). The bottom left panel presents the fractional redshift residual $|\Delta z/(1 + z_{\rm BGS})|$ as a function of $z_{\rm BGS}$, and the bottom right panel presents the normalized $|\Delta z/(1 + z_{\rm BGS})|$ histogram. Overall, BGS redshifts are in excellent agreement with GAMA redshifts. We find that over 99.7% of the overlapping BGS galaxies have $|\Delta z/(1 + z_{\rm BGS})|$ < 0.001. Lan et al. (2023) present a similar assessment of BGS redshifts, but using redshifts from visual inspection in place of GAMA.

An overall >95% redshift success rate for the BGS Bright sample is necessary to achieve the BGS science requirements,
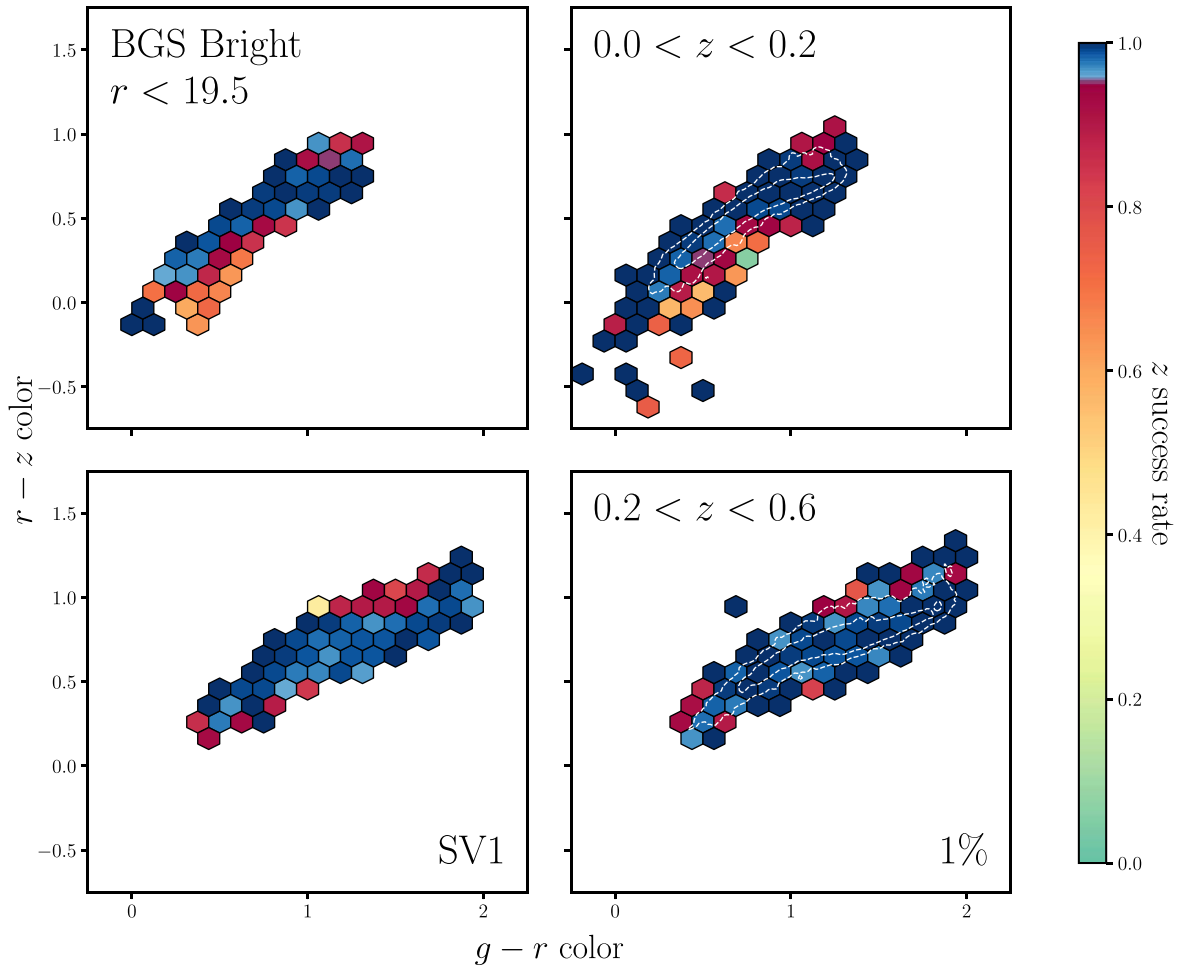
Figure 13. Redshift success rate of BGS Bright galaxies from SV1 (left) and the One-Percent Survey (right) as a function of $g - r$ and $r - z$ colors. The top panels include galaxies with $0.0 < z < 0.2$; the bottom panels include galaxies with $0.2 < z < 0.6$. For reference, we mark the 68th and 95th percentiles of the color distribution of One-Percent Survey BGS Bright galaxies (white contours). The color map represents the z success rate, where redshift success rates above >95% are marked with a blue color mapping. We find slightly lower redshift success rates in the bluest galaxies ($g - r < 0.4$) because they are systematically fainter. Overall, we find a >90% redshift success rate throughout the color space and no strong color dependence for the One-Percent Survey.

based on cosmological forecasts of galaxy clustering analyses. We demonstrate above that we *exceed* this requirement. In fact, we achieve an overall >95% redshift success rate for the BGS Faint sample as well, with the updated selection criteria (Figures 12 and 14). Furthermore, we demonstrate that the BGS Bright sample has a weak $r_{\rm fiber}$ and optical color dependence (Figures 12 and 13). Lastly, we demonstrate that the BGS redshift efficiency does not depend significantly on observing conditions (Figure 15).

5.4. Fiber Assignment Efficiency

As described in Section 4, BGS will observe its footprint with four passes (effective three visits). Targets will be assigned fibers using the `fiberassign` code,[64] where the highest priority for bright time will be given to the BGS Bright targets and 20% of the BGS Faint targets. The other 80% of BGS Faint targets are assigned at a lower priority. To achieve the scientific objectives of BGS, we require a fiber assignment efficiency of >80% for BGS Bright—i.e., >80% of BGS Bright targets must be assigned fibers over the course of the survey.

At the beginning of SV operations, the state and knowledge of the focal plane condition evolved rapidly, including the discovery of poor positioning and faulty electronics. As of 2021 October, 4174 of the 5000 positioners in the focal plane are fully functional and currently being used for science targets. The remaining malfunctioning positioners are currently being used to satisfy the sky fiber budget. The reduction in functional fiber positioners significantly reduces the overall fiber assignment efficiency for DESI. In Figure 17, we present the fiber assignment efficiency of the BGS Bright (blue) and Faint (orange solid) samples as a function of the number of passes for the focal plane status as of 2021 October. We also include the fiber assignment efficiency for the higher-priority (orange dotted–dashed) and lower-priority (orange dotted) BGS Faint targets. Even with the reduced focal plane capabilities, we confirm that with four passes we achieve the >80% fiber assignment efficiency requirement for the BGS Bright sample.

6. BGS Early Data Release

In the previous section, we demonstrated with DESI SV data that BGS will meet its requirements on completeness and redshift efficiency. In the following, we showcase the key
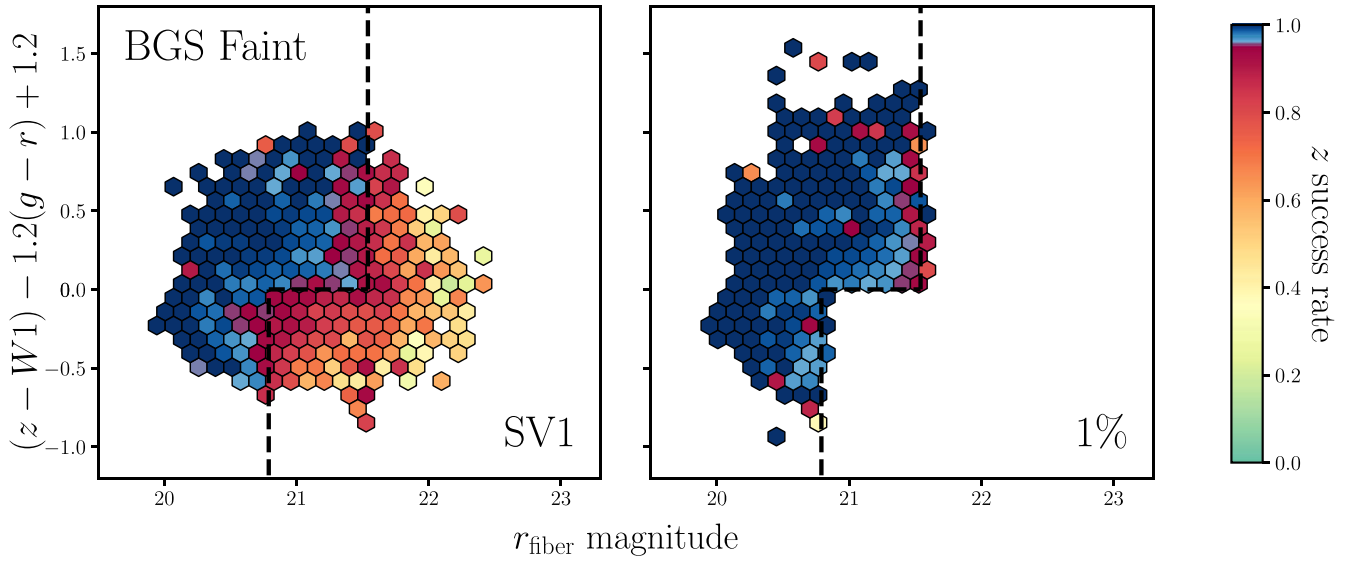

Figure 14. Redshift success rate of the BGS Faint sample as a function of $r_{\rm fiber}$ and $(z - W1) - 1.2(g - r) + 1.2$ color from the SV1 (left) and the One-Percent Survey (right) observations. We mark the $r_{\rm fiber}-$color BGS Faint selection in black dashed and represent the redshift success rate with the color map. The SV1 BGS Faint sample (left) is selected using only a 19.5 mag $< r <$ 20.0 mag cut instead of the $r_{\rm fiber}-$color selection. The redshift success rate of SV1 galaxies outside the $r_{\rm fiber}-$color cut illustrates that the BGS Faint selection is effective at excluding objects with low redshift success and produces a sample with high redshift efficiency.
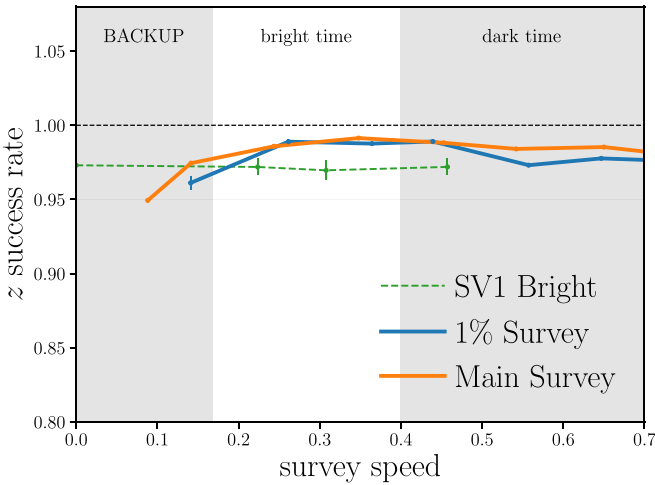
Figure 15. Redshift success rate as a function of "survey speed" for all BGS galaxies in the One-Percent Survey (blue) and main survey (orange). We also include the redshift success rate for the BGS Bright sample from SV1 (green dashed). Survey speed is used to determine whether to observe the bright-time, dark-time, or BACKUP program and is estimated by the Exposure Time Calculator. It is derived from seeing, transparency, air mass, and sky brightness of the exposure and serves as a metric for the observing conditions. The BGS survey speed boundaries are currently defined to be $[\frac{1}{6}, 0.4]$. BGS achieves a redshift success rate above the required >95% threshold throughout its entire survey speed range.

advantages of the BGS galaxy samples based on the first public data set, the Early Data Release (EDR).

In total, DESI amassed redshifts of 285,335 of BGS Bright galaxies and 201,532 BGS Faint galaxies in ∼5 months of operations. DESI acquired ≃4200 redshifts per exposure at a rate of one exposure per 20 minutes on average. Over the next 5 yr, this will expand to an unprecedented >10 million galaxies spanning a third of the sky at 2 mag deeper than the SDSS MGS. In Figure 18, we highlight the progress of BGS and present the absolute number of redshifts in $\Delta z = 0.02$ bins for BGS Bright (left; blue) and Faint (right; orange) galaxies
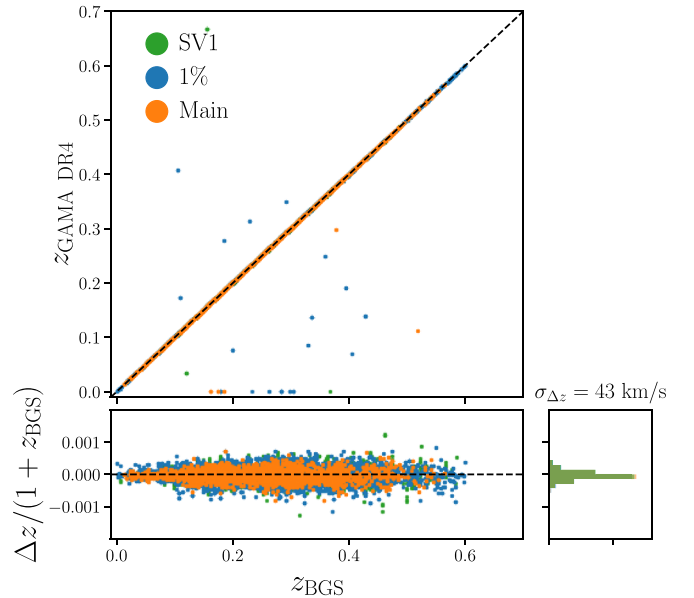
Figure 16. Comparison of BGS redshifts to GAMA redshifts for BGS galaxies from the SV1 (green), One-Percent Survey (blue), and main survey (orange) that are also in GAMA. In the top panel, we plot GAMA redshift, $z_{\rm GAMA}$, vs. BGS redshift, $z_{\rm BGS}$. In the bottom panels, we plot the fractional redshift residual, $\Delta z/(1 + z_{\rm BGS})$, as a function of $z_{\rm BGS}$ (left) and the normalized histogram of $\Delta z/(1 + z_{\rm BGS})$ (right). The comparison only includes high-quality GAMA redshifts with quality flag NQ > 2. Of the ∼25,000 overlapping BGS galaxies, 99.7% have $|\Delta z/(1 + z_{\rm BGS})| < 0.001$. The scatter in the redshift difference between BGS and GAMA is small: $\sigma_{\Delta z} = 43$ km s^{-1}. BGS redshifts show excellent overall agreement with GAMA redshifts.

observed during the SV programs. BGS targeting successfully delivers galaxies spanning the desired redshift range, $0.0 < z < 0.6$. The Bright and Faint samples have median redshifts of $z = 0.2$ and 0.3, respectively, which is more than double that of the SDSS MGS. We include the redshift distribution of GAMA DR4 for comparison. Even with the EDR alone, BGS exceeds the total number of spectroscopic redshift of GAMA.
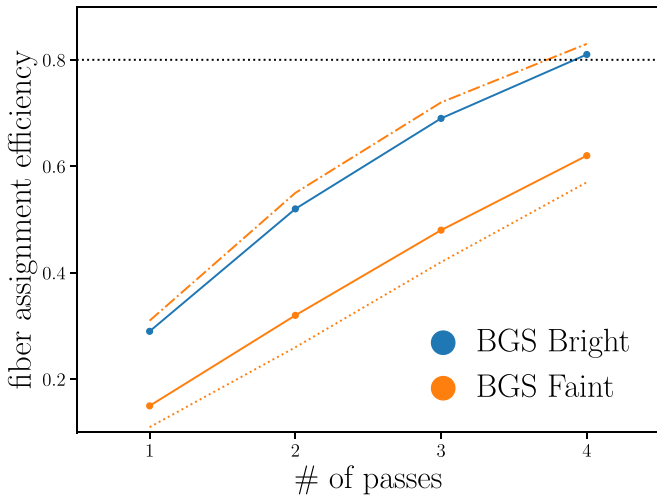
Figure 17. Fiber assignment efficiency of BGS Bright (blue) and Faint (orange) as a function of the number of passes. BGS will be observed with four passes; each position in the footprint will be visited on average three times to ensure the required completeness. The BGS Bright targets and 20% of the BGS Faint targets (orange dotted–dashed) are assigned fibers with the highest priority during bright time. The rest of the BGS Faint targets are assigned lower priorities (orange dotted). We assign higher priorities to a fraction of BGS Faint targets to facilitate corrections for fiber assignment incompleteness in future clustering analyses. The fiber assignment efficiencies are estimated for the focal plane condition as of 2021 October, where 4174 of 5000 fiber positioners are available for science targets. Some of the remaining malfunctioning positioners are used to meet the sky fiber budget. Even if the number of functional positioners does not increase in the future, with four passes we achieve the 80% fiber assignment efficiency requirement for BGS Bright.

In Figure 19, we further highlight the advantages of BGS through its comoving number density distribution, $\bar{n}(z)$. BGS will have significantly higher number density than any previous survey in this redshift range. We include $\bar{n}(z)$ for SDSS (dashed), BOSS (dotted), and GAMA DR4 (dashed–dotted) for comparison. For GAMA DR4, we include galaxies in the GAMA II Main Survey and GAMA I Main Survey (SURVEY_CLASS $> = 3$) with reliable redshifts ($nQ > = 3$). We also include $\bar{n}(z)$ for the DESI dark-time LRGs above $z \gtrsim 0.4$, the redshift limit that will be imposed for LRG galaxy clustering analyses (red). At $z = 0.2$, the BGS number density is more than an order of magnitude larger than SDSS.

7. Summary

Over the next 5 yr, DESI will conduct dark- and bright-time spectroscopic galaxy surveys on the 4 m Mayall Telescope at Kitt Peak National Observatory, using robotically actuated fiber-fed spectrographs that can collect 5000 spectra simultaneously. As the first Stage IV dark energy experiment to be realized, it promises to make unprecedented measurements of cosmic acceleration and advance our understanding of the nature of dark energy. During dark conditions, DESI will measure the redshifts of 20 million LRGs, ELGs, and quasars from $z \approx 0.4$ to 3.0. During bright conditions, DESI will survey the low-redshift universe, $0 < z < 0.6$, when dark energy is most dominant, with >10 million BGS galaxies. By targeting brighter galaxies at closer distances, BGS proceeds effectively in slower conditions and makes optimal use of bright time.

BGS will enable a broad range of science goals from probing dark energy to studying dwarf galaxies. To achieve this, we require BGS to sample a wide range of galaxy types, have a high and well-characterized completeness, and be at least an

order of magnitude larger than SDSS MGS. These requirements translate, in practice, to the following: the primary galaxy sample (BGS Bright) will be selected using a magnitude limit that yields a target density >800 targets deg^{-2}, BGS targets will have a stellar contamination rate of <1%, >80% of BGS Bright targets will be assigned to fibers, and redshifts will be successfully measured for >95% of those assigned fibers. BGS will also cover a footprint of 14,000 deg^2 and complete its 5 yr operations with 20% margins (in ~4 yr) in simulated operations.

In this work, we present the finalized target selection and survey design for BGS. BGS targets are selected from the LS DR9 imaging surveys (DECaLS, BASS, and MzLS), with supplementary data from external catalogs (including Gaia DR2, Tycho-2, and SGA). We apply spatial masking together with fiber magnitude, quality, and bright-end cuts to remove spurious sources and contaminants. We further impose a ($G_{\rm Gaia} - r_{\rm raw}$) > 0.6 cut to remove stars while retaining a high galaxy completeness. From the target set, we select the following samples designed to achieve well-defined goals:

1. *BGS Bright* is the primary sample assigned with highest priority. As a magnitude-limited sample ($r < 19.5$) BGS Bright meets the stated requirements on completeness and density, with ~860 targets deg^{-2}.
2. *BGS Faint* selects fainter galaxies at $19.5 < r < 20.175$ with an additional $r_{\rm fiber}$−color cut to ensure a high redshift efficiency and boost the comoving density. We find the color, $(z - W1) - 1.2(g - r) + 1.2$, to be an accurate proxy for emission-line flux. Hence, the $r_{\rm fiber}$−color cut identifies galaxies faint in r that either have relatively bright fiber magnitudes or have strong emission lines.
3. *BGS AGN* is a supplementary sample of AGN host galaxies that are otherwise rejected by the BGS star–galaxy separation and raise the completeness of the dark-time DESI quasar selection. The primary selection criteria are based on optical and WISE infrared colors that trace the signatures of hot, AGN-heated dust.

We note that the selection criteria above are significantly updated from preliminary versions presented in Ruiz-Macias et al. (2021) and Zarrouk et al. (2021), particularly for BGS Faint. See Section 3 for further information.

After target selection, BGS targets are assigned fibers based on a strategy optimized to ensure the highest completeness for BGS Bright and otherwise maximize the number of successful assignments. We assign in the first priority tier all BGS Bright and 20% of BGS Faint targets. The remaining 80% of BGS Faint and BGS AGN targets are assigned to a lower priority tier. We promote a random subsample of BGS Faint targets to facilitate later corrections for fiber assignment incompleteness. Conflicts caused by cases where multiple targets of the same priority are available to a fiber are resolved by a random subpriority given to each target.

DESI will observe BGS during "slower" conditions, according to a predetermined threshold on "survey speed"—a dynamically calculated metric for the impact of observing conditions derived from seeing, transparency, air mass, and sky brightness. BGS will observe a footprint of 14,000 deg^2 as closely matched to the dark-time program as possible. Each point on the footprint will be visited three times on average, using a four-pass strategy, to ensure a high (>80%) fiber
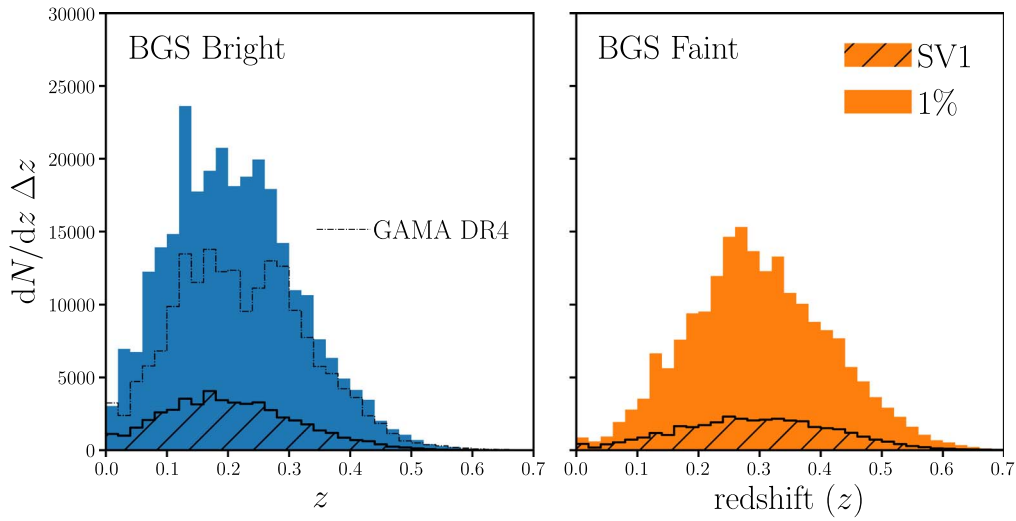
Figure 18. Redshift distribution of BGS galaxies from SV1 (hashed) and the One-Percent Survey (solid). We present the distributions of the BGS Bright and Faint galaxies in the left and right panels, respectively. The success of BGS targeting delivers galaxies in the desired redshift range, $0.0 < z < 0.6$. The Bright and Faint samples have median redshifts of $z \sim 0.2$ and 0.3, respectively. During $\sim$5 months of SV observations, DESI amassed 286,934 BGS Bright and 202,590 Faint BGS redshifts at an average rate of $\simeq$4200 per 20-minute exposure. The BGS Bright sample from SV already exceeds the number of redshifts in GAMA DR4 (dotted–dashed). Over the course of the next 5 yr, BGS will expand to an unprecedented >10 million spectra over a third of the sky.
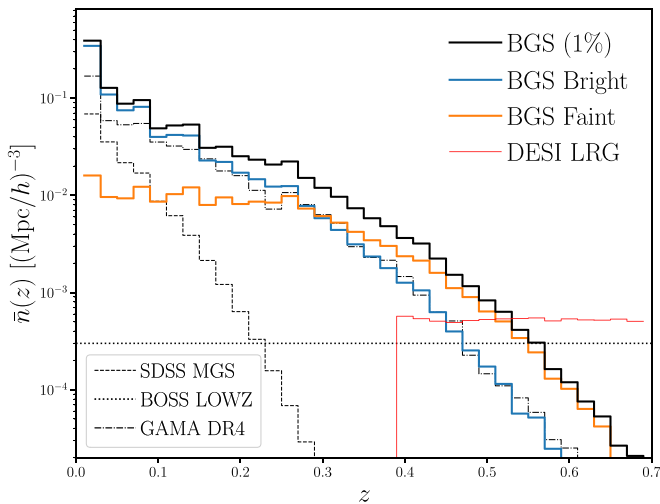
Figure 19. Comoving number density distribution, $\bar{n}(z)$, of BGS galaxies from the EDR (black; SV1 and the One-Percent Survey). We plot $\bar{n}(z)$ for BGS Bright (blue) and Faint (orange). We show external data sets of interest, SDSS (dashed), BOSS (dotted), and GAMA DR4 (dashed–dotted), and DESI LRGs (red) in the overlapping range. BGS will provide the highest-density cosmological galaxy sample to date at low redshifts. It will provide maximum leverage against higher-redshift measurements and CMB constraints for dark energy constraints. Furthermore, its high density and broad galaxy selection will enable a wide range of new approaches to galaxy clustering and galaxy evolution studies.

assignment completeness. Exposure times are dynamically scaled based on the measured observing conditions to yield uniform redshift efficiency and a close-to-homogeneous survey. We set the anchoring exposure time to $t_{\mathrm{nom}} = 180$ s based on spectral simulations. t_{nom} is defined as the exposure time required to achieve >95% redshift efficiency for the BGS Bright sample under nominal dark conditions. Based on forecasts using simulations of survey operations, we confirm that we complete the BGS survey as detailed above in 5 yr with a margin of 20% (Section 4.2).

A primary goal of this work is to demonstrate that these BGS design choices achieve its stated requirements—specifically,

those on target density, redshift efficiency, and fiber assignment efficiency. To do so, we utilize spectroscopic observations from the SV program conducted by DESI before the start of the main survey. SV was divided into the SV1 and One-Percent Survey, observed over $\sim$110 nights (Section 5.1). SV1 aimed to characterize the redshift performance under different observing conditions and optimize the target selection. Meanwhile, the One-Percent Survey aimed to validate the main survey design choices and provide clustering samples of particularly high completeness for additional tests. Using LS imaging data and these SV observations, we have demonstrated in Section 5 the following:

1. Our stellar mask, together with our fiber magnitude, quality, and bright-end cuts, successfully removes spurious sources without significantly impacting the target completeness. Furthermore, we find <1% stellar contamination for BGS targets. Overall, we find <5% variation in the target densities of BGS Bright and Faint samples and no strong dependence on imaging properties (Figures 2 and 8).

2. We achieve the required 95% redshift success rate for the BGS Bright sample with an exposure time of $t_{\mathrm{nom}} = 180$ s under nominal conditions (Figure 11). This redshift efficiency does depend markedly on r_{fiber} and optical colors, as expected, but our target selection achieves a high redshift efficiency for a broad range of galaxies (Figures 12 and 13).

3. We achieve a >95% redshift success rate for the BGS Faint sample using the $r_{\mathrm{fiber}}-$color based selection, which effectively identifies targets with relatively bright r fiber magnitudes or strong emission lines (Figures 12 and 14).

4. We achieve a >95% redshift success rate for both BGS Bright and Faint over the range of survey speeds expected to be available to BGS (Figure 15). This demonstrates that the impact of observing conditions is well understood and that the spectroscopic pipeline is robust to systematic error in challenging conditions.

20

5. Lastly, we achieve $>80\%$ fiber assignment efficiency for the BGS Bright sample with a four-pass strategy (Figure 17). This estimate is based on the focal plane status as of 2021 October, which has $\simeq 4200$ positioners available to science targets. Efforts to fix malfunctioning positioners are ongoing and should ultimately result in a higher fiber assignment efficiency for the same four-pass strategy.

Overall, we have demonstrated that BGS will successfully deliver a >10 million galaxy sample within $0 < z < 0.6$ at a high completeness over a wide range of galaxy properties. As such, BGS will be an order of magnitude larger than the SDSS MGS and will provide the densest galaxy sample out to $z \approx 0.45$ to date. Clustering analyses of BGS galaxies will produce the most precise low-z BAO and RSD measurements, thereby maximizing the leverage against higher-redshift measurements, such as the CMB. BGS presents a unique discovery space for testing the predictions of dark energy and modified gravity models. Furthermore, its high sampling density makes BGS ideal for state-of-the-art analyses using galaxy–galaxy lensing, higher-order statistics, small-scale clustering, and multitracer techniques. In addition, BGS will be an unprecedented sample for studying galaxy formation and decoding the relation between galaxies and dark matter.

Appendix A
SV1 Selection

SV for DESI was divided into two main programs: SV1 and the One-Percent Survey. We primarily focus on the One-Percent Survey in this work, since it used the same target selection as the main survey (Section 3.1), as well as a similar observing strategy (Section 5.1). SV1 provided the prior observations that we used to devise and optimize the One-Percent Survey and final target selection and observing strategy. In this appendix, we describe the target selection that was used for SV1. The observing strategy for the SV1 program is described in Section 5.1 and also in DESI Collaboration et al. (2023, in preparation).

Preliminary BGS target selection established that observing a magnitude-limited BGS Bright sample and a fainter BGS Faint sample would enable a survey that can achieve a broad range of science goals (Ruiz-Macias et al. 2021; Zarrouk et al. 2021). With SV1 observations, we aimed to test more specific choices in the star–galaxy separation, BGS Faint sample selection, and quality cuts. First, for the star–galaxy separation, we wanted to confirm whether the final criterion of excluding Gaia objects with $(G_{\mathrm{Gaia}} - r_{\mathrm{raw}}) \leqslant 0.6$ (Section 3) sufficiently removes stellar contaminants. Therefore, for all SV1 targets, we used a relaxed star–galaxy separation that only excludes Gaia objects that have $(G_{\mathrm{Gaia}} - r_{\mathrm{raw}}) \leqslant 0.6$ and is also best fit by a PSF model in TRACTOR. We also did not impose the FMC (Equation (2)) or the bright limit (Equation (6)).

Next, we designed SV1 to explore the BGS Faint sample selection and whether additional cuts could significantly increase its redshift success rate. In addition to a "Bright" target class that corresponds to the $r < 19.5$ BGS Bright sample, SV1 also included three additional fainter target classes: (1) a "Faint" sample with $19.5 < r < 20.1$ targets that extends 0.1 mag fainter than the preliminary BGS Faint selection, (2) a "Faint extended" sample with even fainter targets $20.1 < r < 20.5$ that also have $r_{\mathrm{fib}} > 21.051$, and (3) a "Faint extended fiber magnitude" sample also with fainter targets, $r > 20.1$, but with brighter fiber magnitudes, $r_{\mathrm{fib}} < 21.051$. The goal of class 1 was to explore the relationship between magnitude and redshift success rate in further detail for the BGS Faint sample. The goal of classes 2 and 3 was to probe whether there are any subsets of fainter galaxies that would produce higher redshift success rates. In
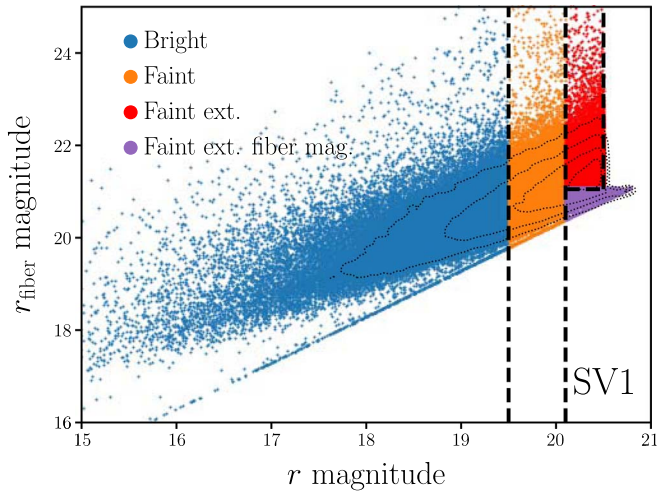
Figure 20. $r_{\rm fib}$ vs. r distribution of SV1 targets in the "Bright" (blue), "Faint" (orange), "Faint extended" (red), and "Faint extended fiber magnitude" (purple) target classes. We mark the r and $r_{\rm fib}$ limits of the target classes in black dashed. Target selection for SV1 was designed to test the star–galaxy separation, BGS Faint sample selection, and quality cuts. Therefore, the SV1 selection, which we present in Appendix A, is overall a more relaxed version of the final BGS target selection (Section 3).

Figure 20, we present the r versus $r_{\rm fib}$ relation of SV1 target classes. The final selection of the BGS Faint sample ($19.5 < r < 20.175$ and $r_{\rm fib}$−color cut) was determined using observations of the fainter SV1 targets.

Lastly, we used SV1 observations to test the preliminary quality cuts from Ruiz-Macias et al. (2021). In addition to the quality cuts in the final selection (Equations (3) and (4)), the preliminary cuts also include cuts based on TRACTOR photometric quality flags: (FRACMASK$_i$ < 0.4) and (FRACIN$_i$ > 0.3) and (FRACFLUX$_i$ < 5). To test whether each of the preliminary quality cuts minimizes spurious targets from photometric artifacts without sacrificing completeness, we include a "Low Quality" target class in SV1. This target class included $r < 20.1$ objects (131 objects deg^{-2}) without any quality cuts. Later, through visual inspection, we confirm that the TRACTOR-based quality cuts remove a significant number of real galaxies, so we exclude them in the final quality cut

(Section 3). When we construct the target catalog for SV1, we randomly sample the targets to meet densities of 300, 50, 50, and 20 targets deg^{-2} for the "Faint," "Faint extended," "Faint extended fiber magnitude," and "Low Quality" classes, respectively.

Appendix B
Bright-time Sky Brightness Model

Survey simulations of DESI operations were a key component of determining the final design and observing strategy of BGS. They simulate the detailed operations of DESI observations and account for expected configuration and dead times of the instrument, as well as historical weather, seasonal, and environmental factors. Nightly operations are simulated as a sequence of tile exposures, where the exposure time is scaled according to the predicted sky brightness at the time of observation. For the dark program, the simulations include a simplified model of sky brightness that is sufficiently accurate for dark time (D. Schlafly et al. 2023, in preparation). However, accurately simulating BGS operations requires a more accurate model of sky brightness during bright time. In this appendix, we describe how we construct this bright-time sky brightness model using an empirical data-driven approach.

To construct our sky brightness model, we use sky spectra primarily observed during SV1. A large number of sky spectra were observed by DESI because a significant number of fibers are dedicated to measuring the sky flux in every exposure to perform sky subtraction in the spectroscopic pipeline (Guy et al. 2023). We only use sky spectra observed by DESI exposures during high transparency and exclude any sky spectra observed during twilight, when the altitude of the Sun is above $-18°$. We supplement the SV1 data with sky spectra measured during the DESI commissioning (CMX) campaign, as well as sky spectra from SDSS-III BOSS (also used in Fagrelius 2018) under similar high transparency and nontwilight conditions. In total, we use sky spectra from 2331 SV1 exposures, 12 CMX exposures, and 990 BOSS exposures. In Figure 21, we present the air mass and lunar conditions of these exposures: DESI SV1 (blue), CMX (orange), and BOSS (green). The exposures span a broad range of observing conditions that fully encompasses typical BGS bright-time conditions.
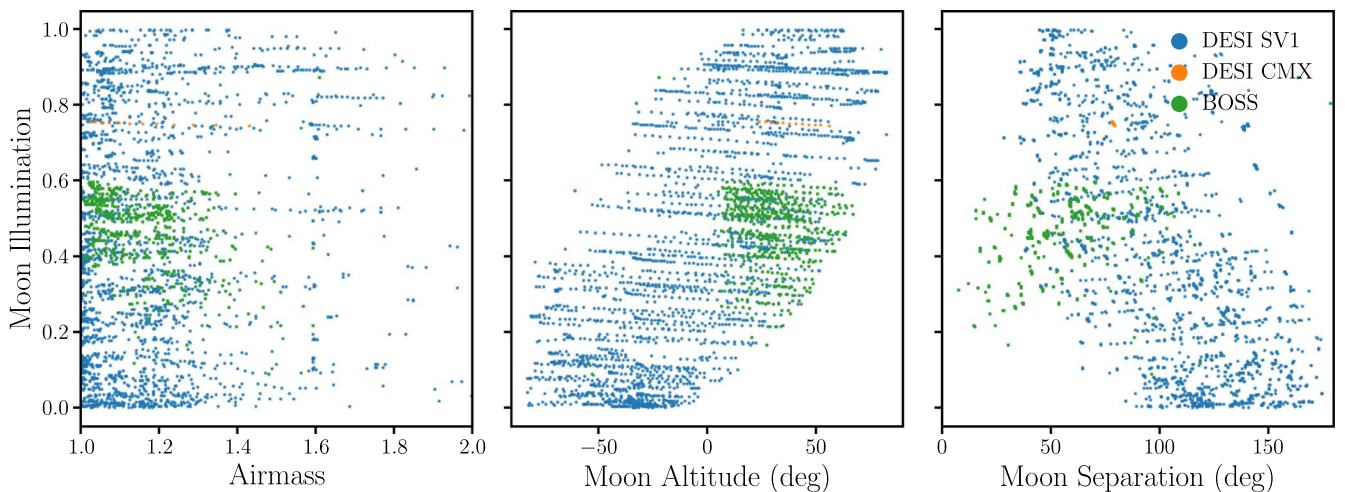
Figure 21. The distribution of air mass and lunar conditions (illumination, altitude, separation) of DESI SV1 (blue), DESI commissioning (CMX; orange), and BOSS (green) sky spectra used to construct the empirical bright-time sky brightness model. The exposures enable us to construct a model that predicts sky brightness given air mass, Moon illumination, altitude, and separation as input.
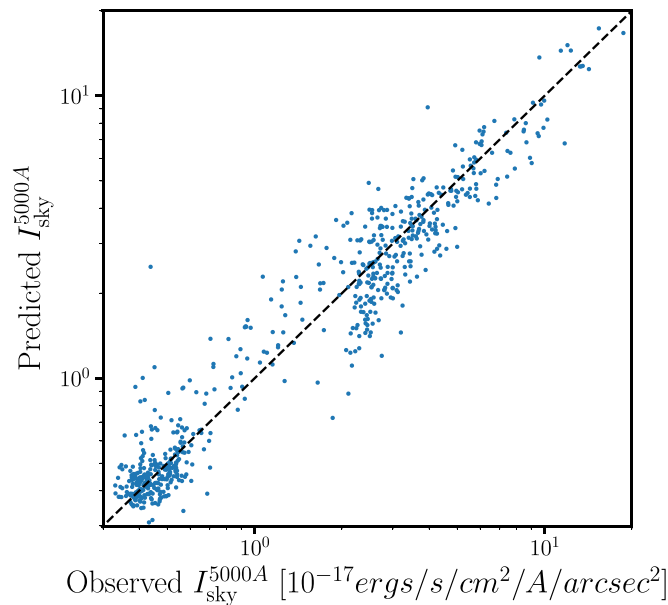
Figure 22. Comparison of predicted sky brightness at 5000 Å, I_{sky}^{5000A}, of the bright-time sky brightness model vs. the observed I_{sky}^{5000A} for a test set of observations. The bright-time sky brightness model is trained using ridge regression on I_{sky}^{5000A} compiled from the exposures in Figure 21. The bright-time sky brightness model shows overall good agreement with observations and, therefore, accurately estimates the sky brightness during bright time.

For each exposure, we compute the median sky spectrum of all the observed sky spectra in the exposure. We then convert the sky spectrum flux to sky surface brightness using the area of the DESI and BOSS fiber apertures. Afterward, we smooth the median sky brightness and estimate its amplitude at 5000 Å, I_{sky}^{5000A}. We use I_{sky}^{5000A} because we find good agreement between the redshift success rates predicted by the spectral simulations (Section 4.1) and those of SV observations when we scale exposure time of the spectral simulations based on this amplitude.

Next, we use the I_{sky}^{5000A}, air mass, Moon illumination, altitude, and separation values of all the exposures to construct our sky brightness model. We use ridge regression to train our model with 80% of the exposures. The other 20% is reserved for testing the model. The L2 regularization in ridge regression helps reduce model complexity and multicollinearity. We train polynomials of different orders (up to 8) and choose one with the minimum cross-validation score. For our sky brightness model, we use a fifth-order polynomial model that takes air mass, Moon illumination, altitude, and separation as inputs and predicts I_{sky}^{5000A}. In Figure 22, we compare the sky brightness, I_{sky}^{5000A}, of observations versus our model for the test set of exposures. Overall, we find good agreement between the bright-time sky brightness model and observations. Moreover, survey simulations for BGS using this sky brightness model are in good agreement with the One-Percent Survey and early main survey operations.

ORCID iDs

ChangHoon Hahn ● https://orcid.org/0000-0003-1197-0902
Omar Ruiz-Macias ● https://orcid.org/0000-0001-8848-9768
Shaun Cole ● https://orcid.org/0000-0002-5954-7903
David H. Weinberg ● https://orcid.org/0000-0001-7775-7261
John Moustakas ● https://orcid.org/0000-0002-2733-4559
Anthony Kremin ● https://orcid.org/0000-0001-6356-7424
Jeremy L. Tinker ● https://orcid.org/0000-0003-3578-6149
Risa H. Wechsler ● https://orcid.org/0000-0003-2229-011X
Steven Ahlen ● https://orcid.org/0000-0001-6098-7247
Shadab Alam ● https://orcid.org/0000-0002-3757-6359
Stephen Bailey ● https://orcid.org/0000-0003-4162-6619
David Brooks ● https://orcid.org/0000-0002-8458-5047
Andrew P. Cooper ● https://orcid.org/0000-0001-8274-158X
Tamara M. Davis ● https://orcid.org/0000-0002-4213-8783
Kyle Dawson ● https://orcid.org/0000-0002-0553-3805
Arjun Dey ● https://orcid.org/0000-0002-4928-4003
Biprateep Dey ● https://orcid.org/0000-0002-5665-7912
Daniel J. Eisenstein ● https://orcid.org/0000-0002-2929-3121
Jaime E. Forero-Romero ● https://orcid.org/0000-0002-2890-3725
Carlos S. Frenk ● https://orcid.org/0000-0002-2338-716X
Enrique Gaztañaga ● https://orcid.org/0000-0001-9632-0815
Julien Guy ● https://orcid.org/0000-0001-9822-6793
Mustapha Ishak ● https://orcid.org/0000-0002-6024-466X
Stéphanie Juneau ● https://orcid.org/0000-0002-0000-2394
Robert Kehoe ● https://orcid.org/0000-0002-7101-697X
Ting-Wen Lan ● https://orcid.org/0000-0001-8857-7020
Martin Landriau ● https://orcid.org/0000-0003-1838-8528
Laurent Le Guillou ● https://orcid.org/0000-0001-7178-8868
Michael E. Levi ● https://orcid.org/0000-0003-1887-1018
Paul Martini ● https://orcid.org/0000-0002-0194-4017
Aaron Meisner ● https://orcid.org/0000-0002-1125-7384
Jundan Nie ● https://orcid.org/0000-0001-6590-8122
Peder Norberg ● https://orcid.org/0000-0002-5875-0440
Nathalie Palanque-Delabrouille ● https://orcid.org/0000-0003-3188-784X
Will J. Percival ● https://orcid.org/0000-0002-0644-5727
Anand Raichoor ● https://orcid.org/0000-0001-5999-7923
Christoph Saulder ● https://orcid.org/0000-0002-0408-5633
Eddie Schlafly ● https://orcid.org/0000-0002-3569-7421
David Schlegel ● https://orcid.org/0000-0002-5042-5088
David Sierra-Porta ● https://orcid.org/0000-0003-3461-1347
Gregory Tarle ● https://orcid.org/0000-0003-1704-0781
Christophe Yèche ● https://orcid.org/0000-0001-5146-8533
Rongpu Zhou ● https://orcid.org/0000-0001-5381-4372
Hu Zou ● https://orcid.org/0000-0002-6684-3997

References

Abbott, T. M. C., Aguena, M., Alarcon, A., et al. 2022, PhRvD, 105, 023520
Albrecht, A., Bernstein, G., Cahn, R., et al. 2006, arXiv:astro-ph/0609591
Alexander, D. M., Davis, T. M., Chaussidon, E., et al. 2023, AJ, 165, 124
Amon, A., Robertson, N. C., Miyatake, H., et al. 2023, MNRAS, 518, 477
Bianchi, D., Burden, A., Percival, W. J., et al. 2018, MNRAS, 481, 2338
Blake, C., Baldry, I. K., Bland-Hawthorn, J., et al. 2013, MNRAS, 436, 3089
Bolton, A. S., & Schlegel, D. J. 2010, PASP, 122, 248
Carrasco, J. M., Evans, D. W., Montegriffo, P., et al. 2016, A&A, 595, A7
Chaussidon, E., Yèche, C., Palanque-Delabrouille, N., et al. 2023, ApJ, 944, 107
Cooper, A. P., Koposov, S. E., Allende Prieto, C., et al. 2023, ApJ, 947, 37
Dark Energy Survey Collaboration, Abbott, T., Abdalla, F. B., et al. 2016, MNRAS, 460, 1270
Dawson, K. S., Schlegel, D. J., Ahn, C. P., et al. 2013, AJ, 145, 10
DESI Collaboration, Abareshi, B., Aguilar, J., et al. 2022, ApJ, 164, 62
DESI Collaboration, Aghamousa, A., Aguilar, J., et al. 2016a, arXiv:1611.00036 [astro-ph]
DESI Collaboration, Aghamousa, A., Aguilar, J., et al. 2016b, arXiv:1611.00037 [astro-ph]
Dey, A., Schlegel, D. J., Lang, D., et al. 2019, AJ, 157, 168
Driver, S. P., Bellstedt, S., Robotham, A. S. G., et al. 2022, MNRAS, 513, 439

Eardley, E., Peacock, J. A., McNaught-Roberts, T., et al. 2015, MNRAS, 448, 3665
Eisenstein, D. J., Weinberg, D. H., Agol, E., et al. 2011, AJ, 142, 72
Eke, V. R., Baugh, C. M., Cole, S., et al. 2004, MNRAS, 348, 866
Fagrelius, P. 2018, PhD thesis, Univ. California, Berkeley, USA
Fang, F., Forero-Romero, J., Rossi, G., Li, X.-D., & Feng, L.-L. 2019, MNRAS, 485, 5276
Flaugher, B., Diehl, H. T., Honscheid, K., et al. 2015, AJ, 150, 150
Gaia Collaboration, Brown, A. G. A., Vallenari, A., et al. 2018, A&A, 616, A1
Gaia Collaboration, Prusti, T., de Bruijne, J. H. J., et al. 2016, A&A, 595, A1
Gil-Marín, H., Percival, W. J., Verde, L., et al. 2017, MNRAS, 465, 1757
Górski, K. M., Hivon, E., Banday, A. J., et al. 2005, ApJ, 622, 759
Guy, Bailey, S., Kremin, A., et al. 2023, AJ, 165, 144
Hahn, C., Kwon, K. J., Tojeiro, R., et al. 2023, ApJ, 945, 23
Hahn, C., Scoccimarro, R., Blanton, M. R., Tinker, J. L., & Rodríguez-Torres, S. A. 2017, MNRAS, 467, 1940
Hahn, C., & Villaescusa-Navarro, F. 2021, JCAP, 2021, 27
Hanuschik, R. W. 2003, A&A, 407, 1157
Heymans, C., Tröster, T., Asgari, M., et al. 2021, A&A, 646, A140
Høg, E., Fabricius, C., Makarov, V. V., et al. 2000, A&A, 355, L27
Kirkby, D., Robitaille, T., Julienguy, et al. 2021, desihub/specsim: August 2020 Release, v0.14, Zenodo, doi:10.5281/zenodo.4566008
Kochanek, C. S., Eisenstein, D. J., Cool, R. J., et al. 2012, ApJS, 200, 8
Lan, T.-W., Tojeiro, R., Armengaud, E., et al. 2023, ApJ, 943, 68
Lang, D., Hogg, D. W., & Mykytyn, D. 2016, ascl soft, Astrophysics Source Code Library, ascl:1604.008
Levi, M., Bebek, C., Beers, T., et al. 2013, arXiv:1308.0847
Li, C., & White, S. D. M. 2009, MNRAS, 398, 2177
Makarov, D., Prugniel, P., Terekhova, N., Courtois, H., & Vauglin, I. 2014, A&A, 570, A13
Mao, Y.-Y., Geha, M., Wechsler, R. H., et al. 2021, ApJ, 907, 85
McDonald, P., & Seljak, U. 2009, JCAP, 2009, 007
McNaught-Roberts, T., Norberg, P., Baugh, C., et al. 2014, MNRAS, 445, 2125
Meisner, A. M., Lang, D., & Schlegel, D. J. 2017a, AJ, 153, 38
Meisner, A. M., Lang, D., & Schlegel, D. J. 2017b, AJ, 154, 161
Miyatake, H., Sugiyama, S., Takada, M., et al. 2022, PRD, 106, 083520

Mohammad, F. G., de la Torre, S., Bianchi, D., Guzzo, L., & Peacock, J. A. 2016, MNRAS, 458, 1948
Moustakas, J., Coil, A. L., Aird, J., et al. 2013, ApJ, 767, 50
Moustakas, J., Lang, D., Schlegel, D. J., et al. 2021, BAAS, 53, 527.04, https://baas.aas.org/pub/2021n1i527p04
Moustakas, J., Zaritsky, D., Brown, M., et al. 2011, arXiv:1112.3300
Myers, A. D., Moustakas, J., Bailey, S., et al. 2023, AJ, 165, 50
Noeske, K. G., Weiner, B. J., Faber, S. M., et al. 2007, ApJL, 660, L43
Planck Collaboration, Aghanim, N., Akrami, Y., et al. 2020, A&A, 641, A6
Raichoor, A., Moustakas, J., Newman, J. A., et al. 2023, AJ, 165, 126
Rezaie, M., Seo, H.-J., Ross, A. J., & Bunescu, R. C. 2020, MNRAS, 495, 1613
Ross, A. J., Samushia, L., Burden, A., et al. 2014, MNRAS, 437, 1109
Ruiz-Macias, O., Zarrouk, P., Cole, S., et al. 2021, MNRAS, 502, 4328
Schlegel, D. J., Finkbeiner, D. P., & Davis, M. 1998, ApJ, 500, 525
Schubnell, M., Ameel, J., Besuner, R. W., et al. 2016, Proc. SPIE, 9908, 990892
Secrest, N. J., Dudik, R. P., Dorland, B. N., et al. 2015, ApJS, 221, 12
Seljak, U. 2009, PhRvL, 102, 021302
Seljak, U., Aslanyan, G., Feng, Y., & Modi, C. 2017, JCAP, 2017, 009
Silber, J. H., Fagrelius, P., Fanning, K., et al. 2023, AJ, 165, 40
Smith, A., He, J.-h., Cole, S., et al. 2019, MNRAS, 484, 1285
Strauss, M. A., Weinberg, D. H., Lupton, R. H., et al. 2002, AJ, 124, 1810
Tinker, J., Wetzel, A., & Conroy, C. 2011, arXiv:1107.5046
Tremonti, C. A., Heckman, T. M., Kauffmann, G., et al. 2004, ApJ, 613, 898
Verga, M. 2017, The OpenNGC object list with the main metadata, OpenNGC, doi:10.21938/Y.1EJWUD_MQ6B_EDFOVBBW
Wang, Y., & Zhao, G.-B. 2020, RAA, 20, 158
Wright, E. L., Eisenhardt, P. R. M., Mainzer, A. K., et al. 2010, AJ, 140, 1868
Xu, H., Zheng, Z., Guo, H., et al. 2018, MNRAS, 481, 5470
York, D. G., Adelman, J., Anderson, J. E., Jr., et al. 2000, AJ, 120, 1579
Zarrouk, P., Ruiz-Macias, O., Cole, S., et al. 2021, MNRAS, 509, 1478
Zhai, Z., Tinker, J. L., Becker, M. R., et al. 2019, ApJ, 874, 95
Zhou, R., Dey, B., Newman, J. A., et al. 2023, AJ, 165, 58
Zou, H., Zhou, X., Fan, X., et al. 2017, PASP, 129, 064101
Zu, Y., & Mandelbaum, R. 2015, MNRAS, 454, 1161
Zu, Y., Weinberg, D. H., Jennings, E., Li, B., & Wyman, M. 2014, MNRAS, 445, 1885